DAXX safeguards heterochromatin formation in embryonic stem cells

Antoine Canat, Adeline Veillet, Renaud Batrin, Clara Dubourg, Priscillia Lhoumaud, Pol Arnau-Romero, Maxim Greenberg, Frédéric Bonhomme, Paola Arimondo, Robert Illingworth, et al.

DAXX safeguards heterochromatin formation in embryonic stem cells

Antoine Canat[1,‡], Adeline Veillet[1], Renaud Batrin[1], Clara Dubourg[1,§], Priscillia Lhoumaud[2], Pol Arnau-Romero[2], Maxim V. C. Greenberg[2], Frédéric Bonhomme[3], Paola B. Arimondo[3], Robert Illingworth[4], Emmanuelle Fabre[1], Pierre Therizols[1,*,‡]

[1]Université de Paris, Laboratoire Génomes, Biologie Cellulaire et Thérapeutiques, CNRS UMR7212, INSERM U944, Institut de Recherche St Louis, F- 75010 Paris, France
[2]Université Paris Cité, CNRS, Institut Jacques Monod, F-75013 Paris, France.
[3]Institut Pasteur, Université Paris Cité, CNRS, Epigenetic Chemical Biology, UMR 3523, F-75724 Paris, France
[4]Centre for Regenerative Medicine, Institute for Regeneration and Repair, The University of Edinburgh, Edinburgh BioQuarter, 5 Little France Drive, Edinburgh EH16 4UU, United Kingdom.

[*]Author for correspondence: pierre.therizols@cnrs.fr Tel: +33-1-5727-8926
[‡]Present address: Institute of Epigenetics and Stem Cells, Helmholtz Zentrum München, München, Germany
[§]Present address: Université de Paris, Epigenetics and Cell Fate, CNRS, 75013 Paris, France

Abstract

Genomes comprise a large fraction of repetitive sequences folded into constitutive heterochromatin to protect genome integrity and cell identity. *De novo* formation of heterochromatin during preimplantation development is an essential step for preserving the ground-state of pluripotency and the self-renewal capacity of embryonic stem cells (ESCs). Yet, the molecular mechanisms responsible for the remodeling of constitutive heterochromatin are largely unknown. Here, we identify that DAXX, an H3.3 chaperone essential for the maintenance of ESCs in the ground state, accumulates in pericentromeric regions independently of DNA methylation. DAXX recruits PML and SETDB1 to promote the formation of heterochromatin, forming foci that are hallmarks of ground-state ESCs. In the absence of DAXX or PML, the 3D-architecture and physical properties of pericentric and peripheral heterochromatin are disrupted, resulting in derepression of major satellite DNA, transposable elements and genes associated with the nuclear lamina. Using epigenome

editing tools, we observe that H3.3, and specifically H3.3K9 modification, directly contribute to maintaining pericentromeric chromatin conformation. Altogether, our data reveal that DAXX is crucial for the maintenance and 3D-organization of the heterochromatin compartment and protects ESC viability.

Keywords: Heterochromatin; Pericentromere; Chromocenters; Nuclear periphery; histone variant H3.3; DAXX; SETDB1; PML; Embryonic Stem Cell

Introduction

Eukaryotic nuclei generally contain two major genomic compartments, referred to as A and B, which respectively contain the active and inactive fractions of the genome. At the chromosome level, these compartments are characterized by alternating gene-rich and gene-poor domains. The B compartment is composed primarily of repetitive sequences, with satellite tandem repeats comprising one of the most abundant classes. Pericentromeric regions in mouse are composed of tandem repeats of a 234 bp sequence, named Major Satellite, that constitute approximately 8 Mb on each chromosome (Consortium et al., 2002; Guenatri et al., 2004). Most genes and repeated sequences of the B compartment are transcriptionally repressed by cooperative epigenetic mechanisms leading to the formation of constitutive heterochromatin. The three-dimensional organization of constitutive heterochromatin is an important layer regulating transcription (Falk et al., 2019; Lu et al., 2021). In some species, including the mouse, the pericentromeric heterochromatin (PCH) of different chromosomes aggregates to form large DAPI-dense heterochromatin clusters, called chromocenters. Disruption of satellite clustering is often associated with increased DNA damage and defects in chromosome segregation that are seen in pathologies such as Alzheimer's disease and breast cancer (Hahn et al., 2013; Jagannathan et al., 2018; Mansuroglu et al., 2016; Zhu et al., 2011). Gene-poor domains are preferentially found beneath the nuclear edge and often referred as Lamina-Associated Domains (LADs) (Guelen et al., 2008). The tethering to the nuclear envelope is stochastic, and LADs are also found associated with other nuclear landmarks such as chromocenters and nucleoli (Koningsbruggen et al., 2010; Wijchers et al., 2015).

At the molecular level, constitutive heterochromatin exhibits covalent modifications including DNA methylation, H3K9 and H4K20 trimethylation (H3K9me3 and H4K20me3). Maintenance of H3K9me3 at pericentromeric satellites relies on the SUV39H1/2 methyltransferases, whereas a distinct H3K9me3 methyltransferase, SETDB1, operates at dispersed DNA

repeats and telomeres (Fukuda et al., 2018; Gauchier et al., 2019; Martens et al., 2005; Matsui et al., 2010).

Heterochromatin maintenance is intrinsically linked to chromatin replication during S phase, but also requires the incorporation of histone variants, such as macroH2A and H3.3, into chromatin independently of DNA synthesis (Buschbeck and Hake, 2017; Mendiratta et al., 2019). The histone variant H3.3 differs from the canonical histone H3 by 4 or 5 residues and is deposited throughout the cell cycle in active and inactive chromatin by different histone chaperones. These histone-binding proteins prevent promiscuous incorporation into chromatin (Szenker et al., 2011). Together with ATRX, DAXX forms a histone chaperone complex responsible for H3.3 incorporation into heterochromatin regions, including PCH, retrotransposons and telomeres (Drané et al., 2010; Elsässer et al., 2015; He et al., 2015; Lewis et al., 2010; Sadic et al., 2015). At telomeres and retrotransposons, DAXX promotes heterochromatin formation by recruiting SUV39H1/2 or SETDB1, hereby facilitating the deposition of H3K9me3 (Elsässer et al., 2015; Gauchier et al., 2019; He et al., 2015; Hoelper et al., 2017). In addition to its role in H3.3 deposition, DAXX also prevents promiscuous incorporation of H3.3 by recruiting soluble H3.3-H4 dimers to PML nuclear bodies, membrane-less hubs for post-translational modification of proteins (Delbarre et al., 2013; Delbarre et al., 2017; Lallemand-Breitenbach and Thé, 2018).

Heterochromatin is *de novo* established during early embryogenesis, involving an important remodeling of its molecular composition and 3D-organization (Burton and Torres-Padilla, 2014). However, the underlying mechanisms and their functional relevance for early development remain elusive. During preimplantation development, the DNA methylation inherited from parental gametes is erased and reaches its minimal level in the blastocyst, defining the ground-state of pluripotency (Leitch et al., 2013; Ying et al., 2008). This wave of DNA demethylation directly leads to the transcriptional upregulation of several repetitive sequences, a process that is essential for the remodeling of constitutive heterochromatin (Jachowicz et al., 2017; Lu et al., 2021; Probst et al., 2010). For instance, the upregulation of major satellite transcripts at the 2-cell stage is required for PCH reorganization into chromocenters and normal developmental progression (Casanova et al., 2013; Probst et al., 2010). Yet, derepression of DNA repeats correlates with high DNA damage signaling and their prolonged expression results in developmental arrest, suggesting that silencing through a DNA methylation-independent mechanism is required for normal embryogenesis (Jachowicz et al., 2017; Ziegler-Birling et al., 2009). Polycomb group proteins were previously shown to bind and facilitate silencing of repetitive sequences upon DNA hypomethylation (Saksouk et al., 2014; Tosolini et al., 2018; Walter et al., 2016). However, knockout of most polycomb-related genes does not impact pre-implantation embryogenesis

(Aloia et al., 2013), implying that other factors maintain heterochromatin in the absence of DNA methylation.

In mouse, both DAXX and H3.3 deletions cause genomic instability resulting in early embryonic lethality with most knockout embryos failing to reach the blastocyst stage (Jang et al., 2015; Liu et al., 2020; Michaelson et al., 1999). DAXX binds major satellite regions during the earliest stages of development, just before PCH reorganizes to form chromocenters (Arakawa et al., 2015; Liu et al., 2020). While the importance of DAXX for chromocenter formation remains unknown, the viability of *Daxx*$^{-/-}$ embryos drops after chromocenter formation (Liu et al., 2020; Probst et al., 2010), suggesting a direct link between DAXX function at chromocenters and developmental progression. Surprisingly, *Daxx* is not required for *in vitro* culture of blastocyst-derived Embryonic Stem Cells (ESCs) (Elsässer et al., 2015; He et al., 2015; Hoelper et al., 2017). In ESCs, DAXX is not recruited to PCH, but rather to retrotransposons and telomeres (Elsässer et al., 2015; Gauchier et al., 2019; He et al., 2015; Saksouk et al., 2014). However, the recruitment of DAXX to chromatin is tightly associated with the low level of DNA methylation that characterize preimplantation embryogenesis (Arakawa et al., 2015; He et al., 2015; Liu et al., 2020). ESCs are typically cultured in serum-based media and accumulate high levels of DNA methylation (Leitch et al., 2013), which could explain the discrepancies with *in vivo* observations. ESCs can maintain low levels of DNA methylation and reach the ground-state of pluripotency when grown in a serum-free medium, named 2i, but the role of DAXX for their survival and the formation of PCH has yet to be addressed.

Here, we decipher the role played by DAXX at PCH in pluripotent ESCs. We find that DAXX is essential for ground-state ESC survival. We provide evidence that DAXX localizes to pericentric heterochromatin and recruits PML and SETDB1, facilitating heterochromatin formation and organization through H3.3K9 modification. The deletion of *Daxx* or *Pml* impacts pericentromeric heterochromatin formation altering its biophysical and clustering properties. Thus, our results identify DAXX as an essential regulator preserving heterochromatin integrity and maintaining the viability of ground-state ESCs.

Results

DAXX is essential for ESC survival upon ground-state conversion.

To assess the role of DAXX in pluripotent cells, we generated a *Daxx* knock-out (KO) ESC line. We targeted exon 3 of *Daxx* using CRISPR/cas9 technology. While we confirmed the absence of DAXX mRNA and protein (Fig. 1A; Fig. S1A), there were no obvious changes in

H3.3 protein levels in the resulting *Daxx* KO ESC line (Fig. 1A). Consistent with previous reports, loss of DAXX did not impact the growth of ESCs cultured with a serum-based medium (Elsässer et al., 2015). Likewise, neural differentiation induced by leukemia inhibitory factor withdrawal and retinoic acid addition did not impact on cell viability in *Daxx* KO ESCs (Diff., Fig. 1B). When the *Daxx* KO and WT ESCs were converted to the ground state, using a medium with two small kinase inhibitors and vitamin C (hereafter denoted 2iV), *Daxx* KO cells showed no growth defect and a similar decrease in DNA methylation after 4 days of conversion (Fig. 1B; Fig. S1B). However, prolonged culture in 2iV medium induced a drastic decrease in cell viability (Fig. 1B). Compared to the parental WT ESCs, only 12.6% of *Daxx* KO ESCs remained after 8 days of culture in 2iV (Fig. 1B). No surviving cells could be detected after 9 to 10 days of conversion. Altogether, these results indicate an essential role for DAXX in the maintenance of pluripotent cell survival upon ground-state conversion.

To further investigate the impact of *Daxx* knockout, we monitored the transcriptional landscapes under different conditions using RNA sequencing (RNA-seq). Upon differentiation with retinoic acid, our analysis reveals a rather minor differential expression of protein-coding genes between *Daxx* KO and WT cells, with only 8 and 125 genes exhibiting up- and downregulation respectively (Fig. S1C). We concluded that the absence of DAXX only has a minor impact on transcription upon neural differentiation. This result is consistent with the absence of morphological or cell growth defects observed and confirms that DAXX is dispensable for neuronal differentiation. After 4 days of 2iV conversion a substantial differential expression of genes in *Daxx* KO and WT ESCs was observed (Fig. S1C). To ask whether the drop in viability observed in *Daxx* KO ESCs upon prolonged 2iV culture was resulting from a ground-state conversion defect, we compared the expression of 166 markers previously identified as differentially expressed during this process (Blaschke et al., 2013). For both cell lines most of these markers changed expression upon conversion according to the expected pattern (Fig. S1D) supporting the conclusion that *Daxx* KO ESCs can reach the ground-state of pluripotency after 4 days of 2iV conversion.

Overall, our data show that *Daxx* is essential for the survival of ground-state ESCs but their loss of viability is unlikely caused by a conversion defect. As we could not identify any significant gene networks that might explain the subsequent loss of viability in Daxx KO ESCs, it is plausible that DAXX may play a role in regulating the repressed regions of the genome.

DAXX contributes to the transcriptional repression of DNA repeats and peripheral heterochromatin.

As DAXX is known to be responsible for H3.3 deposition in heterochromatic regions, we investigated the impact of *Daxx* deletion on the transcriptional repression of the silenced portion of the genome (Elsässer et al., 2015).

LADs make up a significant portion of the silenced compartment. To investigate the effect of *Daxx* deletion on the expression of genes located in the 1180 LADs described in ESCs (Peric-Hupkes et al., 2010), we compared their expression to that of genes with a more central positioning, away from the nuclear lamina (CEN). In serum and differentiated conditions, we found that LAD and non-LAD genes shared a very similar expression profile (Fig. 1C; Fig. 1D). However, we observed an increase in the mRNA levels of several LAD genes normally silenced such as *Casp1*, *Casp4*, and *Casp12* on chromosome 9 and *Naip6* and *Naip5* on chromosome 13, in *Daxx* KO ESCs under 2iV condition (Fig. 1C). Genome-wide, the differential expression of genes located in LADs was significantly increased in the 2iV condition, suggesting that the presence of DAXX is necessary for proper silencing of these genes in ground-state ESCs (Fig. 1D).

Histone modification H3K9me2 is a hallmark of LADs and generally accumulates along the nuclear envelope (Kind et al., 2013; Peric-Hupkes et al., 2010). To assess whether the global upregulation of LAD genes observed in *Daxx* KO ESCs upon 2iV conversion was associated with a defect in peripheral heterochromatin assembly, we examined the accumulation of H3K9me2 by immunofluorescence. In WT and *Daxx* KO ESCs grown in serum condition, the H3K9me2 signal was irregularly diffuse in the nucleoplasm with a significant accumulation at the nuclear edge (Fig. 1E). Quantification of H3K9me2 distribution by linescan density did not show any significant difference in the enrichment of signal at the nuclear periphery between WT and *Daxx* KO ESCs in serum (Fig. 1F; Fig. S1E). However, after 4 days of 2iV conversion, the H3K9me2 signal remained enriched at the nuclear rim in WT converted cells, but only small patches along the nuclear periphery were observed in the absence of DAXX (Fig. 1E). Linescan quantification confirmed a significant decrease in H3K9me2 enrichment at the nuclear periphery in *Daxx* KO ESCs grown in 2iV (Fig. 1F). In contrast, LaminB1 accumulated normally at the nuclear edge in both cell lines regardless of growing conditions, indicating no global nuclear lamina assembly defects in *Daxx* KO ESCs (Fig. S1F). We therefore conclude that DAXX is necessary for the maintenance of peripheral heterochromatin.

Overall, our observations show that *Daxx* deletion impacts the regulation of the nuclear periphery by altering the tethering of peripheral heterochromatin and the transcriptional silencing of genes located in LADs.

DAXX relocates to chromocenters upon ground-state conversion.

We additionally found that many endogenous retrovirus families were upregulated in *Daxx* KO ESCs in serum and 2iV (Fig. 2A), consistent with previous observations (Elsässer et al., 2015; He et al., 2015). Several LINE1 elements, notably the L1MdT and L1MdA families, not previously reported as DAXX targets, were also upregulated in pluripotent *Daxx* KO ESCs. The role of DAXX on transcriptional silencing was not limited to interspersed repeats as we detected a strong upregulation of major satellites RNA in both serum and 2iV condition in the *Daxx* KO cells.

To investigate whether DAXX binds to major satellites in ESCs, we used immunofluorescence with H3K9me3 staining to track PCH after confirming the strong correlation between H3K9me3 and major satellites using immuno-FISH (Fig. S2A; Fig. S2B). In both serum and 2iV conditions, DAXX signal concentrated in the nucleoplasm as round foci (Fig. 2B; Fig. S2C). The distribution of foci sizes was similar in both growing conditions, but a small fraction of larger foci could be observed under 2iV condition. We therefore set a threshold defining small and larger DAXX foci (Fig. S2D). The large DAXX foci exhibited higher levels of DAPI and H3K9me3 specifically under 2iV condition, supporting that DAXX could relocate to PCH in ground-state ESCs (Fig. S2E; Fig. S2F). To confirm this observation, we segmented nuclei and PCH foci using DAPI and H3K9me3 signals, respectively, allowing us to measure the enrichment of DAXX signal at PCH per nuclei (Fig. S2G). The level of DAXX observed at PCH upon 2iV conversion was significantly higher than in the serum condition (Fig. 2C). Notably, the increase in DAXX enrichment in 2iV was not homogenous among the H3K9me3 foci population, but rather the result of a subset of clusters showing strong DAXX enrichment, allowing us to determine a threshold to define DAXX-positive PCH (Fig. 2D). While only 14% of cells showed one DAXX-positive PCH cluster in the serum condition, 83% of 2iV-converted cells had at least one DAXX-positive H3K9me3 focus (Fig. 2E). A small proportion of cells showed 2 or 3 or more DAXX-enriched PCH foci (16% and 5%, respectively). Interestingly, our analysis revealed that DAXX-enriched PCH foci were bigger in size and had higher H3K9me3 staining intensities, suggesting a potential link between DAXX and H3K9me3 regulation (Fig. 2F; Fig. 2G).

Altogether, our data show that DAXX accumulates in a subset of PCH clusters in ground-state ESCs, suggesting that it may play a role in the maintenance of PCH and the transcriptional silencing of major satellite sequences.

DNA methylation cycle does not influence DAXX recruitment at PCH

The DAXX/ATRX complex is recruited to the telomeric regions in the context of DNA hypomethylation, a characteristic typically seen in ground-state ESCs (He et al., 2015). We questioned if the accumulation of DAXX at PCH could be caused by the decreased level of DNA methylation. We first explored the role of the active demethylation pathway, which shows increased activity in 2iV conditions (Blaschke et al., 2013). The presence of vitamin C stimulates the TET enzymes, which convert 5-methyl cytosine (5mC) into 5-hydroxymethyl cytosine (5hmC). We performed a knockout of both *Tet1* and *Tet2* in mESCs using Crispr-Cas9 to create a cell line devoid of these 2 proteins (Fig. S3A; Fig. S3B). The Liquid Chromatography tandem with mass spectrometry (LC-MS-MS) analysis confirmed that no detectable 5hmC was present in the *Tet1/2* DKO ESCs in either serum or 2iV conditions, with only slight differences noted in 5mC levels (Fig. 3A; Fig. 3B).

Upon monitoring DAXX and PCH localization in *Tet1/2* DKO ESCs grown in serum, or after 4 days of 2iV conversion, immunofluorescent detection showed that the absence of 5hmC minimally affected DAXX localization (Fig. 3C). Similar to WT ESCs, *Tet1/2* DKO ESCs showed an increase in DAXX signal at a subset of PCH following 2iV conversion (Fig. 3D; Fig. 3E). Indeed, 83.3% of nuclei showed at least one DAXX-positive PCH foci, with a slightly higher proportion exhibiting 2 DAXX-positive PCH foci than in WT. These findings suggest that the relocation of DAXX to PCH during ESCs ground-state conversion does not rely on the active demethylation pathway.

To investigate further the role of DNA methylation, we analyzed the association of DAXX with PCH in triple knockout ESCs for *Dnmt1*, *Dnmt3a*, and *Dnmt3b* (Dnmt TKO) (Dubois et al., 2022). Without the presence of DNA methyltransferase, neither 5mC nor 5hmC could be detected by LC-MS/MS (Fig. 3A; Fig. 3B). Similar to the patterns observed in both the WT and Tet1/2 DKO, the level of DAXX at PCH significantly increased in 2iV conditions, with a nearly identical proportion of DAXX-positive foci (Fig. 3D; Fig. 3E).

In conclusion, the recruitment of DAXX to PCH in ground-state ESCs is neither a consequence of 5mC loss nor does it require the active DNA demethylation pathway. Instead, these findings suggest that the presence of DAXX at PCH could be a distinct hallmark of ground-state ESCs.

DAXX maintains pericentric heterochromatin organization in pluripotent cells.

To investigate the role that DAXX might play at PCH in ground-state ESCs, we next investigated whether DAXX facilitates PCH formation in ESCs. Since the loss of pericentromeric silencing is generally caused by defective heterochromatin assembly and often correlates with impaired clustering of chromocenters (Hahn et al., 2013; Healton et al., 2020; Pinheiro et al., 2012; Zhu et al., 2011), we performed DNA FISH experiments against the major satellites and segmented the 3D signal to determine the number of clusters (Fig. 4A). In serum or differentiated cells, the deletion of *Daxx* had no significant impact on the number of clusters (Fig. 4B). However, after 4 days of 2iV conversion, the average number of major satellite foci was increased by 37% in the *Daxx* KO ESCs. The presence of an increased number of PCH foci indicates that DAXX is required for their clustering in ESCs, specifically under 2iV condition and correlates with the loss of viability observed in these cells at later stages of conversion (Fig. 1B). To confirm the role of DAXX in PCH clustering, we used the TALE (transcription activator–like effector) epigenome editing tool to ask whether direct DAXX recruitment to major satellites was sufficient to reduce the number of foci. We generated a FLAG-tagged TALE engineered to specifically target major satellite sequences (hereafter called $TALE_{MajSat}$), following the design of a previous study (Miyanari et al., 2013). Immunofluorescence against the FLAG tag of the $TALE_{MajSat}$ confirmed its colocalization with the major satellite FISH signal (Fig. 4C). When bound to pericentromeres in pluripotent *Daxx* KO cells, $TALE_{MajSat}$-DAXX restored chromocenter clustering, leading to a decrease in the number of PCH foci (Fig. 4D). In WT ESCs, artificial tethering of DAXX to chromocenters had a similar impact, increasing endogenous PCH clustering (Fig. S4A). These results indicate that DAXX enhances physical interactions between major satellite sequences and contributes to the 3D organization of PCH.

We hypothesized that the decreased chromocenter clustering seen in *Daxx* KO ESCs might result from defective heterochromatin formation. Functional heterochromatin forms a self-segregating subcompartment with limited protein exchange with the rest of the nucleoplasm (Hinde et al., 2015; Strom et al., 2017). To test whether DAXX is important for heterochromatin segregation, we followed GFP-HP1α using live-imaging in WT and *Daxx* KO ESCs (Fig. 4E). We monitored the mobility of GFP-HP1α by measuring its fluorescence recovery rate at chromocenters after photobleaching (Fig. 4E; Fig. S4B). Compared to WT, the half-recovery time was significantly shorter in *Daxx* KO cells both in serum and 2iV conditions, suggesting higher protein exchange between chromocenter and the nucleoplasm in the absence of DAXX (Fig. 4F). However, the mobile fraction of GFP-HP1α remained constant in both cell lines, suggesting that the same amount of protein was bound to chromatin (Fig. S4B).

The boundary property of PCH is known to cause high variance in HP1α signal over time at the edge of a chromocenter, a property visible in condensates due to an increase in coordinated movement of molecules at the border of the compartment (Strom et al., 2017). We reasoned that this higher HP1α recovery rate might arise from altered heterochromatin acting as a barrier to protein diffusion. We thus quantified temporal changes in GFP-HP1α signal intensity variation at unbleached chromocenters (Fig. 4G). We found that variance levels were low in the nucleoplasm of WT ESCs and only increased at chromocenters, peaking at their borders (Fig. 4G; Fig. 4H), confirming previous observations (Strom et al., 2017). However, in *Daxx* KO cells, the pattern of the variance from HP1α signal was altered. In both serum and 2iV conditions, the peak of variance at the edge of chromocenters was significantly lower in the absence of DAXX, suggesting a compromised heterochromatin barrier (Fig. 4H). Moreover, molecular analysis using MNase digestion revealed that *Daxx* deletion in pluripotent ESCs increased the accessibility of pericentric chromatin, indicating that PCH exists in an abnormal state in these cells (Fig. S4C).

Our data collectively suggests that DAXX is important for regulating the compaction state and chromocenter boundary properties of PCH in ESCs. Specifically, in ground-state conditions, DAXX maintains major satellite clustering. In conclusion, DAXX is essential for proper assembly and spatial organization of pericentromeric heterochromatin in pluripotent ESCs.

PML and DAXX share similar roles in ESCs.

PML, identified as a partner of DAXX, has been recently shown to contribute to the transcriptional repression of transposable elements in ESCs (Tessier et al., 2022). To investigate the role of PML in the organization of the heterochromatic compartment in ground-state ESCs, we first analyzed its localization in relation to DAXX and H3K9me3 by immunofluorescence (Fig. 5A). Regardless of culture conditions, PML formed small round foci in the nucleoplasm (Fig. 5A). These are the same nuclear bodies where DAXX accumulates as evidenced by strong Pearson correlation values between the two proteins (Fig. 5A; Fig. S5A). Upon 2iV conversion, a fraction of larger PML foci were observed with higher levels of H3K9me3 and DAPI (Fig. S5B; Fig. S5C; Fig. S5D). These larger PML foci accumulated around PCH in the form of either complete or partial structures, referred to as PML-rim or PML-arc, respectively (Fig. 5A; Fig. S5E). Both the PML-rim and PML-arc structures were consistently associated with the presence of DAXX at PCH and were observed in similar proportions as DAXX-positive PCH clusters (Fig. 2E; Fig. 5B). This indicates that PML is recruited to PCH alongside DAXX in ground-state ESCs.

To further examine the role played by PML at PCH clusters, we analyzed the distribution of major satellites in *Pml* KO ESC using FISH (Tessier et al., 2022). In *Pml* KO ESCs, no protein was detectable (Fig. S5F). Similar to the *Daxx* KO line, *Pml* KO ESCs showed a significant increase in the number of major satellite foci only after 4 days of 2iV conversion (Fig. 5C; Fig. 5D), suggesting that PML, like DAXX, is required for proper PCH clustering in ground-state ESCs.

Next we wished to determine if Pml deficiency influenced the integrity of peripheral heterochromatin. Immunofluorescence revealed that H3K9me2 accumulated at the nuclear periphery to a greater extent in serum conditions in *Pml* KO cells compared to WT cells (Fig. 5E; Fig. 5F). However, after 4 days of 2iV conversion, the H3K9me2 signal in *Pml* KO cells was similar to that observed in *Daxx* KO cells, with only small patches of H3K9me2 present beneath the nuclear envelope and a significant reduction in peripheral enrichment of the signal (Fig. 5F). In contrast, LaminB1 signal was not altered by *Pml* deletion supporting the conclusion that it is specific to peripheral heterochromatin (Fig. S5G; Fig. S5H). To determine how this peripheral heterochromatin alteration influenced gene expression, we analyzed the transcriptional repression of 25 LAD genes that were significantly upregulated, in our RNA-sequencing, following *Daxx* deletion (Fig. 1C, 1D). Out of the 25 selected genes, 22 showed higher mRNA levels in 2iV-converted Pml KO ESCs compared to WT cells when analyzed by RT-qPCR (Fig. 5G). Nonetheless, the transcriptional upregulation in *Pml* KO cells was less pronounced than in *Daxx* KO cells, with 15 genes exhibiting a $\log_2$ fold change exceeding 2, compared to 23 genes in the absence of DAXX. Our findings suggest that PML, like DAXX, plays a role in the transcriptional silencing of LAD genes in ground-state ESCs.

The deletion of *Pml* and *Daxx* have very comparable consequences on the heterochromatin of ESCs after 4 days of 2iV conversion. We thus wondered how *Pml* deletion would impact the viability of ESCs under prolonged 2iV conversion (Fig. 5H). After 4 days of conversion, the viability of *Pml* KO was not impacted, but was decreased by nearly 75% after 8 days. Like the deletion of *Daxx*, this effect was specific to prolonged 2iV conversion as the absence of PML had no consequence on the viability under serum condition or after retinoic acid differentiation.

Overall, our data show that PML and DAXX play similar roles in ground-state ESCs. Like DAXX, PML is recruited to PCH and its absence impairs the proper organization of the heterochromatic compartment, significantly impacting cell viability.

DAXX recruits SETDB1 to chromocenters in ground-state ESCs.

We have shown that in ground-state ESCs, DAXX and PML are recruited to major satellites thereby facilitating PCH formation. To further investigate the mechanism underlying the function of DAXX and PML, we searched for DAXX- and PML-interacting factors that could be recruited specifically to chromocenters. Amongst the DAXX interacting partners, SETDB1, an H3K9me3 methyltransferase, colocalizes with DAXX at PML nuclear bodies and is important for repetitive DNA transcriptional silencing (Cho et al., 2011; Karimi et al., 2011). SETDB1 partially colocalized with PML in a DAXX-independent manner in serum conditions (Fig. S6A). Under 2iV treatment, SETDB1 relocalized to PCH with DAXX and PML in 70% of WT ESCs (Fig. 6A; Fig. 6B; Fig. S6B). By contrast, PML and SETDB1 were only associated with PCH in 5 and 17% of *Daxx* KO cells, respectively (Fig. 6B). We conclude that DAXX is critical for PML and SETDB1 recruitment to chromocenters. To investigate whether DAXX was sufficient for SETDB1 recruitment to PCH, we expressed $TALE_{MajSat}$, fused to DAXX in *Daxx* KO ESCs. TALE-mediated DAXX binding to major satellite repeats drastically increased the amount of SETDB1 signal observed at chromocenters (Fig. 6C; Fig. 6D).

To determine whether SETDB1 was depositing the H3K9me3 modification at PCH when it is recruited by DAXX, we used *Suv39H1/2* double knock-out (Suv39dKO) ESCs (Lehnertz et al., 2003; Peters et al., 2001). As H3K9me3 in WT ESCs is primarily deposited by SUV39H1/2, these Suv39dKO cells provide a system where any detected H3K9me3 can only be attributed to SETDB1 activity. Suv39dKO cells displayed no growth defects in 2iV medium, underscoring the non-essential role of these enzymes for pluripotency. Unlike in WT ESCs, Suv39dKO did not show an accumulation of H3K9me3 at major satellite foci (Fig. 6E; Fig. 6F). However, upon 2iV conversion, we observed a notable accumulation of H3K9me3 in certain major satellite foci surrounded by PML, suggesting that the fraction of SETDB1 recruited to PCH in the ground state is indeed functionally active (Fig. 6E; Fig. 6F).

In summary, our data demonstrate that DAXX recruits PML and SETDB1 to chromocenters, providing an alternative pathway for the deposition of H3K9me3 at PCH in ground-state ESCs.

H3K9me3 is not sufficient to PCH clustering.

Considering our observations that DAXX presence at PCH correlated with higher H3K9me3 levels (Fig. 2G), and its function in the recruitment of SETDB1 (Fig. 6E; Fig. 6F), we asked if *Daxx* deletion would impact the level of H3K9me3 at PCH. Surprisingly, the level of H3K9me3 at PCH was very similar in *Daxx* KO and WT ESCs in serum and 2iV condition

(Fig. S6C; Fig. S6D). These findings suggest that the recruitment of SETDB1 by DAXX is not essential for maintaining H3K9me3 in ground-state.

To better understand the specific roles of DAXX, SETDB1, and H3K9me3 in organizing PCH, we used the $TALE_{MajSat}$ strategy to specifically target these elements to chromocenters in Suv39dKO ESCs. (Fig. 7A). Both histone methyltransferases were able to individually restore H3K9me3 at chromocenters, when targeted by $TALE_{MajSat}$ (Fig. 7A; Fig S6E). The specific recruitment of DAXX to major satellite foci also promoted H3K9me3 deposition via SETDB1, at 70% of chromocenters. The impact of the different $TALE_{MajSat}$ fusions on PCH clustering was further assessed by quantifying the number of TALE-bound foci (Fig. 7B). Consistent with our observations in *Daxx* KO and WT ESCs (Fig. 4D, S4A) targeting DAXX to major satellite also enhanced PCH clustering in Suv39dKO ESCs as evidenced by the reduced number of PCH foci (Fig. 7B). However, the recruitment of either SETDB1 or SUV39H1 did not affect the number of chromocenters, supporting the conclusion that H3K9me3 modification does not influence PCH clustering (Fig. 7B).

In conclusion, the alternative pathway for H3K9me3 deposition at PCH, mediated by DAXX and SETDB1, is not essential for preserving this epigenetic mark. Moreover, the influence of DAXX on PCH organization cannot be solely attributed to SETDB1 or H3K9me3, underscoring a pivotal role for DAXX in PCH organization in ground-state ESCs.

H3.3K9 modification is crucial for PCH organization

Since DAXX, unlike SETDB1, had a direct impact on the spatial organization of chromocenters, we examined the role of its H3.3 chaperone activity by expressing a mutated form, $DAXX^{Y222A}$,

that lowers its interaction with H3.3 (Elsässer et al., 2012). We confirmed that co-immunoprecipitation of $TALE_{MajSat}$ $DAXX^{Y222A}$ fusion with H3.3 was drastically reduced compared to its wild-type counterpart (Fig. S7A). While targeting DAXX to chromocenters could recruit a tagged version of H3.3, neither the control $TALE_{MajSat}$-Δ nor $TALE_{MajSat}$ $DAXX^{Y222A}$ fusion were able to mobilize H3.3 to PCH (Fig. S7B). When expressed in Suv39dKO ESCs, the $TALE_{MajSat}$ $DAXX^{Y222A}$ fusion did not rescue H3K9me3 levels at chromocenters (Fig. 7A; Fig. S7C). This could be attributed to the absence of SETDB1, given the $DAXX^{Y222A}$ mutant's inability to recruit SETDB1 in Daxx KO ESCs (Fig. S7D). Most importantly, did not change the number of chromocenters arguing that H3.3 is crucial for DAXX-mediated PCH clustering (Fig. 7B). To further confirm a function for H3.3 in chromocenter organization, we depleted endogenous H3.3 using a pool of siRNAs targeting

the 3'UTR of H3f3a/b mRNAs and expressed $TALE_{MajSat}$-DAXX in *Daxx* KO ESCs (Fig. 7C; Fig. S7E). The H3.3 knock-down was rescued by the expression of different HA-tagged versions of H3.3, which were assessed for their impact on PCH clustering by immuno-FISH (Fig. 7C; Fig. S7E). The binding of DAXX at major satellite did not enhance PCH clustering when H3.3 was knocked down (Fig. 7D). The expression of a wild-type H3.3-HA significantly reduced the number of major satellite foci and rescued the PCH hyperclustering phenotype mediated by $TALE_{MajSat}$-DAXX. In contrast, expression of $H3.3^{G90M}$, a mutant unable to bind DAXX (Elsässer et al., 2012; Hoelper et al., 2017), did not decrease the number of major satellite foci (Fig. 7D). This result is consistent with the absence of a chromocenter clustering phenotype in cells transfected by $TALE_{MajSat}$- $DAXX^{Y222A}$ (Fig. 7B) and confirms the important role of H3.3 in PCH clustering. Since DAXX can recruit SETDB1 to PCH, we asked whether a H3.3K9 mutant that cannot be methylated impacts PCH clustering and used $H3.3^{K9A}$. Like $H3.3^{G90M}$, $H3.3^{K9A}$ failed to rescue the hyper-clustering phenotype in $TALE_{MajSat}$-DAXX expressing cells, suggesting that the modification of this residue is essential for the spatial organization of chromocenters (Fig. 7D).

Altogether, we conclude that the role of DAXX in PCH organization is intrinsically linked to its chaperone activity. Interaction with H3.3 and H3.3K9 modifications are important in facilitating the spatial organization of pericentromeres in pluripotent ESCs.

Discussion

During early embryogenesis, adapting heterochromatin to compensate for the wave of DNA demethylation is essential to maintain transcriptional repression of repetitive DNA and protect genome integrity. The mechanisms and molecular factors responsible for heterochromatin reorganization were, however, largely unknown. Here, we describe a novel and essential role for the H3.3-chaperone DAXX and its partner PML in the survival of ground-state pluripotent stem cells. Taken together, our results support a model in which DAXX and PML facilitate both pericentric and peripheral heterochromatin formation in ground-state ESCs (Fig. 8). At PCH, DAXX deposits H3.3 and recruits PML and SETDB1, which can methylate H3.3K9. In the absence of either DAXX or PML, PCH is compromised (Fig. 8). In *Daxx* KO ESCs, heterochromatin at major satellite is less compact and partially loses its boundary properties leading to defective chromocenter clustering. At the nuclear periphery, PML and DAXX are necessary for the maintenance of the heterochromatin positioned beneath the nuclear envelope, contributing to the transcriptional silencing of genes tethered to the nuclear lamina. The global failure in heterochromatin compartment formation could directly contribute to the inability of *Daxx* KO and *Pml* KO ESCs to maintain the ground-state of pluripotency.

DAXX and H3.3 impact chromocenter organization

Both DAXX and H3.3 are essential for early embryogenesis, but their specific functions have remained elusive (Jang et al., 2015; Lin et al., 2013; Liu et al., 2020; Michaelson et al., 1999). We found that DAXX is necessary for maintaining the spatial organization and chromatin state of pericentric heterochromatin (PCH), thereby protecting the viability of ground-state ESCs (Fig. 4B; Fig. 4F; Fig. 4H). This finding is consistent with *in vivo* observations, which show that DAXX and SETDB1 are recruited to PCH just before chromocenter formation, and the viability of *Daxx* KO embryos drops quickly after the transition to the pluripotent stage (Arakawa et al., 2015; Cho et al., 2012; Liu et al., 2020). These observations support our conclusion that the role of DAXX and SETDB1 at PCH might be crucial for the ground-state of pluripotency. Since defective PCH assembly is often associated with genomic instability, our model may also explain why *H3f3a/b* double knockout ESCs exhibit severe chromosome segregation defects (Jang et al., 2015).

While *Daxx* deletion had no impact on major satellite transcription and chromocenter formation upon neuronal differentiation (Fig. 2A; Fig. 4B), DAXX and H3.3 are important for chromocenter clustering during myoblast differentiation (Park et al., 2018; Salsman et al., 2017). In myoblasts, DAXX is recruited to chromocenters, where H3.3 deposition stimulates transcription of major satellites, suggesting a mechanism different to the one we observed in ESCs. Different DAXX and partner recruitment pathways could explain the opposite impact of DAXX and H3.3 on major satellite transcription. In ESCs, DAXX recruits SETDB1, thus favoring a repressive chromatin environment. Upon myoblast differentiation, *Setdb1* is downregulated and might not be available for interaction with DAXX, which is recruited to major satellite repeats by the muscle-specific lncRNA ChRO1 (Park et al., 2018; Song et al., 2015).

Recent insights into chromocenter organization have come from the observation that the intrinsically disordered regions of HP1α facilitate the compartmentalization of chromocenters through liquid-liquid phase separation (Larson et al., 2017; Strom et al., 2017). Since the first fifty amino-acids and the C-terminal half of DAXX are intrinsically disordered (Escobar-Cabrera et al., 2010), it is possible that DAXX may also undergo liquid-liquid phase separation. Multivalent interactions between chromodomains recognizing H3K9me3 have also been proposed to contribute to phase separation of heterochromatin (Wang et al., 2019)(Wang et al., 2019). Yet, *Daxx* deletion impacted the boundary properties of pericentromeric heterochromatin without affecting H3K9me3 (Fig. 4H; Fig. S6D). Further, upon 2iV conversion, the fraction of chromocenters bound by DAXX display higher levels of H3K9me3 (Fig. 2D). It has been well documented that HP1 binding to H3K9me3 relies on its

chromodomain (Bannister et al., 2001; Lachner et al., 2001; Mattout et al., 2015). Interestingly, in specific cases, it was observed that the histone variant H3.3 was tri-methylated on its lysine 9 and was required to maintain H3K9me3 levels detected at telomeres (Udugama et al., 2015). Since DAXX-mediated chromocenter clustering relies on H3.3K9 modification (Fig. 7C; Fig. 7D), future work will compare the interaction of HP1α and additional heterochromatin-related proteins to H3.3K9me3 vs. H3K9me3.

Mechanism of DAXX targeting to pericentric heterochromatin

In ground-state ESCs, DAXX binds only a subset of chromocenters in approximatively 80% of cells (Fig. 2E). Given that chromocenters replicate synchronously during mid-S phase (Guenatri et al., 2004), the recruitment of DAXX is unlikely to rely on replicative chromatin remodeling. Polycomb group proteins have been shown to be recruited to PCH in ESCs (Pailles et al., 2022; Saksouk et al., 2014; Tosolini et al., 2018). The fact that DAXX was shown to rely on PRC1 to bind major satellites in zygotes would support a polycomb-mediated recruitment of DAXX in ground-state ESCs (Liu et al., 2020). However, the presence of H3K27me3, deposited by PRC2, is relatively homogenous amongst the PCH foci within a nucleus, suggesting another mechanism (Saksouk et al., 2014; Tosolini et al., 2018).

ESCs, especially grown in 2iV, are characterized by reduced levels of 5mC. Within this context, DAXX has been demonstrated to play a significant role in the formation of heterochromatin at DNA repeat regions (Elsässer et al., 2015; He et al., 2015). However, the absence of DNA methylation was not sufficient to recruit DAXX to PCH, corroborating a previous PCH proteomic analysis (Fig. 3D; Fig. 3E) (Saksouk et al., 2014). Nevertheless, the potential requirement for lower DNA methylation in DAXX recruitment to PCH cannot be excluded, since *Dnmt* TKO ESCs may have evolved adaptive mechanisms during their establishment, possibly explaining discrepancies in PCH epigenetic regulation between *in vitro* and *in vivo* conditions (Pailles et al., 2022).

DNA damage may also be a factor in the recruitment of DAXX to PCH. Several studies have described the incorporation of H3.3 after DNA damage (Adam et al., 2013; Fortuny et al., 2021; Juhász et al., 2018; Li and Tyler, 2016; Luijsterburg et al., 2016). Both HIRA and DAXX-ATRX complexes have been proposed to deposit H3.3 after DNA damage, but DAXX has been more specifically observed at chromocenters damaged by UVC (Fortuny et al., 2021). *In vivo*, DAXX binds preferentially paternal chromosomes which are actively demethylated by the TET enzymes, a pathway that can result ultimately in a DSB (Nakatani et al., 2015; Wossidlo et al., 2011). Since TET enzymes are particularly active in ground-

state ESCs (Blaschke et al., 2013), it was tempting to hypothesize that these enzymes might drive DAXX recruitment to PCH. However, our data compellingly indicate that TET enzymes are not key players in DAXX recruitment (Fig. 3D), suggesting that if a DNA damage response is involved, it may be triggered by a different source of damage. Pericentromeric regions are particularly susceptible to the formation of four-stranded guanine-rich structures in vivo known as G-quadruplexes (Henderson et al., 2017). Intriguingly, ATRX, a partner of DAXX, is known to safeguard heterochromatin from G-quadruplex formation, primarily by recruiting SETDB1 (Teng et al., 2021). While these links provide interesting insights into the potential mechanisms of DAXX recruitment and DNA damage control, they highlight the need for further studies to confirm these hypotheses.

Role of SETDB1 at chromocenters in ground-state ESCs

SETDB1 has been shown to be responsible for H3K9me3 deposition at transposable elements and telomeres (Elsässer et al., 2015; Gauchier et al., 2019; Karimi et al., 2011). Yet, knocking down SETB1 in Suv39h1/h2 double knock-out cells destabilizes chromocenters suggesting that SETDB1 could be involved in PCH formation (Pinheiro et al., 2012).

Our work demonstrates that DAXX is essential for the recruitment of SETDB1 to PCH (Fig. 6A; Fig. 6B). This finding is consistent with a recent study that has highlighted DAXX's role in the histone chaperone network, where it recruits histone methyltransferases, including SETDB1, and promotes H3K9me3 catalysis on new histone H3.3-H4 before DNA deposition (Carraro et al., 2023). However, in ESCs lacking Suv39h1/h2, SETDB1 fails to restore H3K9me3 across all PCH clusters, with restoration only apparent at PML-positive foci (Fig. 6E; Fig. 6F) This finding implies that SETDB1 may preferentially modify histones already integrated into DNA. In contrast to SUV39H1/H2, SETDB1 contains a triple Tudor domain recognizing the double modification K14 acetylation and K9 methylation that may facilitate its binding to hyperacetylated, newly incorporated histone H3.3 (Jurkowska et al., 2017).

In mouse embryonic fibroblasts, SETDB1 promotes H3K9me1 at major satellites in (Loyola et al., 2009). However, SETDB1 was specifically recruited during S-phase by the H3.1/H3.2 chaperone, CAF1, suggesting that SETDB1 substrate specificity might change depending on its recruitment pathway. Similar to our data in ESCs, CAF1 recruited SETDB1 to chromocenters only in a subset of S-phase cells. Since pericentromeric satellites were shown to be particularly sensitive to replicative stress, SETDB1 recruitment could also result from DNA damage (Crosetto et al., 2013).

The role of DAXX and H3.3 upon DNA hypomethylation

This study reveals that DAXX is recruited to pericentromeres in the context of DNA hypomethylation. While PML nuclear bodies are generally devoid of chromatin, PML formed a shell around DAXX-positive chromocenters in hypomethylated ground-state ESCs (Fig. 5A). Similar structures have been observed in patients with immunodeficiency, centromeric instability and facial dysmorphia (ICF) syndrome associated with mutations in DNA methyltransferases (Luciani et al., 2006). In patient lymphocytes, DAXX and DNA repair proteins accumulate at hypomethylated pericentromeric satellites, suggesting that our proposed model could apply to other pathologies (Fig. 8).

In conclusion, our study reveals DAXX as an important factor for different heterochromatic compartments in ground-state ESCs. At the nuclear periphery, DAXX and its partner PML are necessary for the clustering of peripheral heterochromatin at the nuclear edge. At PCH, DAXX deposits H3.3 and recruits PML and SETDB1 to facilitate chromocenter formation by enhancing their clustering properties. It would be interesting to characterize whether DAXX also contributes to the 3D-organization of other heterochromatin domains, such as the clustering of LINE1 elements (Lu et al., 2021). Beyond early development, our work could also provide critical insights into the molecular pathways that overcome DNA hypomethylation transitions in pathological contexts, such as cancers.

Material and Methods

Cell lines

Feeder-free E14 mES cells were used for most experiment excepts otherwise notified. E14 mES cells were kindly provided by Pablo Navaro (Pasteur Institute). *Daxx* KO and Tet1/2 DKO cell lines were constructed using CRISPR/cas9 editing in E14 mES cells. Guide-RNA targeting *Daxx* was designed using the online CRISPOR tool (Sg-mDaxx: gGACCTCATCCAGCCGGTTCA). Guide-RNA targeting *Tet1* and *Tet2* were selected based on a previous study (Mulholland et al., 2020). Oligos were designed with a BbsI site on 5' to clone them into the pSpCas9(BB)-2A-Puro(pX459) v2.0 vector (Ran et al., 2013). *Pml* KO and Dnmt TKO ESCs were generated by CRISPR from E14 cells and described in previous studies (Dubois et al., 2022; Tessier et al., 2022). Feeder-free Suv39HdKO and corresponding WT R1 ES cells were provided by Alice Jouneau and generated in Antoine Peters's laboratory (Lehnertz et al., 2003).

Culture conditions

Pluripotent cells were cultured either in a serum condition, defined as follow: DMEM (Gibco), supplemented with 10% of ESC-certified FBS (Gibco), 2-mercaptoethanol (0.05mM, Gibco), Glutamax (Gibco), MEM non-essential amino acids (0.1mM, Gibco), Penn-Strep (100units/mL, Gibco) and LIF (1000units/mL,) for serum condition. Serum-cultivated cells were grown on 0.1% gelatin-coated plates or stem cell plates (Stem Cell technology) at 37°C with 5% CO2. Medium was changed every day and cells were passaged every 2 to 3 days. The other culture condition is the chemically defined serum-free 2i condition defined as follow: Neurobasal:DMEM/F-12 (50:50, Gibco) medium, supplemented with N2 and B-27 supplements (Gibco), BSA fraction V (0.05%Gibco), 1-thioglycerol ($1.5x10^{-4}$M, Sigma) and ESGRO 2 inhibitors (GSK3i and MEKi) and LIF (Merck). Vitamin C (L-ascorbic acid 2-phosphate, Sigma) was added at a concentration of 100µg/mL (Blaschke et al., 2013). Cells were grown on 0.1% gelatin-coated plates. Medium was changed daily. Cells were passed every 2 days at 1:4 ratio for the first passage then at a 1:6 ratio. Differentiation of mES cells was done by LIF removal for the first 24h. Then, non-LIF medium was supplemented with retinoic acid (10^{-6}M,) for 4 days.

Cell growth was quantified by plating ESCs at a density of 2.10^5 cells/ml in serum and 4.10^5 cells/ml in 2iV every two days. To assess cell numbers, cell counts were performed 3 times using a hemocytometer. Specifically, the number of cells in *Daxx* KO and *Pml* KO ESCs was compared to wild-type (WT) samples, and the relative cell count was expressed as a percentage.

All cell lines are available upon request.

Vectors and transfections

Cells were harvested using trypsin and one million was plated in a 0.1% gelatin-coated plate and transected with 0.2 to 2.5µg of DNA using the Lipofectamine 2000 reagent (Thermo), following manufacturer's protocol. TALE vectors were constructed using previously described methods (Ding et al., 2013). A TALE specific DNA binding domain targeting *Major Satellite* repeats was created by the modular assembly of individual TALE repeats inserted into a backbone vector containing TALE-Nrp1-VP64 previously described (Therizols et al., 2014). The BamHI-NheI fragment containing VP64 was removed to generate the control vector containing only the DNA binding domain (T_{MS}-Δ). VP64 fragment was also replaced by PCR products encoding the DAXX protein, corresponding DAXX mutants or additional proteins such as SUV39H1 and SETDB1. CDS of the different proteins were amplified by PCR from

cDNAs obtained after RNA extraction of serum E14 mES cells. DAXX mutants were generated by PCR from WT DAXX.

For the overexpression H3.3 and derivative mutants, dsDNA blocks (Eurofins Genomics) containing the coding sequences of the murine H3f3b, mH3f3b^{G90M}, mH3f3b^{K9A} and digested by BsmBI were cloned into a pCAGG vector digested by EcoRI and NheI.

All plasmids are available upon request.

RNA extraction for RNAseq or RT-qPCR

Total RNA was extracted using RNeasy extraction kit (Qiagen) according with manufacturer's protocol including DNAseI treatment for 15min at room temperature (Qiagen). Complementary DNA were generated from 1µg of RNA using the Maxima first strand cDNA synthesis kit (Thermo Fisher), with a second round of DNAseI from the Maxima kit for 15min. Real-time qPCR was carried out using a LightCycler 480 instrument (Roche) and the LightCycler 480 SYBR green master mix (Roche). The qRT-PCR primers used in this study are listed in supplementary table. Three independent biological repeats were obtained for each sample. For RNAseq experiment, RNA quality was assessed using the Agilent 2100 bioanalyzer. Libraries were prepared using oligo(dT) beads for mRNA enrichment, then fragmented and reverse transcribed using random hexamers primer. After adaptor ligation, the double-stranded cDNA is completed through size selection of 250-300bp and PCR amplification, then quality of the library is assessed by the Agilent 2100 bioanalyzer. Sequencing was performed in 150bp paired-end reads using an Illumina sequencer platform.

RNA-seq Mapping and Processing

FASTQ files generated by paired end sequencing were aligned to the mouse genome using bowtie2 v2.2.6 (parameters: --local --threads 3; mm9 genome build). Mapped RNA-seq data was processed using tools from the HOMER suite (v4.8). SAM files were converted into tag directories using 'makeTagDirectory' (parameters: -format sam -sspe). Genomic intervals which extended beyond the end of the chromosomes was removed using 'removeOutOfBoundsReads.pl'. bigWig browser track files were generated using 'makeUCSCfile' (parameters: -fsize 1e20 -strand + -norm 1e8). For gene expression analysis, read depths were quantified for all annotated refseq genes using analyzeRepeats.pl (parameters: rna mm9 -strand both -count exons -rpkm -normMatrix 1e7 -condenseGenes). For repeat analysis, read coverage was quantified for each repeat and then condensed to a

single value for each named entry (parameters: repeats mm9 -strand both -rpkm -normMatrix 1e7 -condenseL1). Read depths were then corrected for the number of instances of each repeat prior to expression analysis.

Expression Analysis

Quantified RNA-seq data was processed using the limma package (R/Bioconductor)(Team, 2017). Following the addition of an offset value (1 RPKM) to each gene or repeat, data was normalised across all samples using 'normalizeBetweenArrays' with method='quantile'. Fold-changes and p-values for differential expression of genes and repeats were determined using empirical Bayes statistics. Briefly, data was fit to a linear model using 'lmFit' and specified contrasts were applied using 'makeContrasts' and 'contrasts.fit'. Data was processed using the 'topTable' function with adjust.method="BH" (Benjamini-Hochberg multiple-testing correction). Differential expression was defined as log2 fold change ≤-1 or ≥ 1 and an adjusted p-value of ≤ 0.01. Three biological replicates for each condition represent independently cultured pools of cells.

Data visualization

Heatmaps and boxplots were generated using Prism GraphPad (v9). Histograms were drawn using either Prism GraphPad or Excel. Volcano plots were generated using the plot function in R.

DNA methylation analysis: LC-MS/MS

Genomic DNA was extracted with RNase A as described above, plus an additional digestion step: 1 microgram of DNA was treated with 10U DNA Degradase Plus (ZymoResearch) at 37°C for 4 hours, followed by inactivation of the enzyme at 70°C for 20 minutes and then Amicon Ultra-0.5 mL 10 K centrifugal filters (Merck Millipore) were used to filter the solution. The reaction mixture retained on the centrifuge filter was processed for LC-MS/MS analysis; analysis of total 5-mdC and 5-hmdC concentrations was performed using a Q exactive mass spectrometer (Thermo Fisher Scientific). The instrument was equipped with an electrospray ionization source (H-ESI II Probe) coupled to an Ultimate 3000 RS HPLC (Thermo Fisher Scientific). A ThermoFisher Hypersil Gold aQ chromatography column (100 mm * 2.1 mm, 1.9

µm particle size) heated to 30°C was injected with digested DNA. The flow rate was set to 0.3 ml/min and the column was run for 10 minutes in isocratic eluent consisting of 1% acetonitrile in water containing 0.1% formic acid. Parent ions were fragmented in positive ion mode, parallel reaction monitoring (PRM) mode at 10% normalized collision energy; MS2 resolution was 17,500, AGC target was 2e5, maximum injection time was 50 ms, and separation window was 1.0 m/z. The inclusion list contained the following masses: dC (228.1), 5-mdC (242.1), and 5-hmdC (258.1). Extracted ion chromatograms (±5 ppm) of basic fragments were used for detection and quantification (dC: 112.0506 Da; 5-mdC: 126.0662 Da; 5-hmdC: 142.0609). Calibration curves were previously generated using synthetic standards in the ranges of 0.2 to 10 pmol injected for dC and 0.02 to 10 pmol for 5mdC and 5hmdC. Results were expressed as % of total dC.

Immunofluorescence

Murine ES cells were harvested with trypsin (Gibco) and plated for 4-12h onto either 0.1% gelatin-coated or ECMatrix-coated (Sigma) glass cover slips. Cells were fixed with 4% paraformaldehyde for 10min at room temperature, then rinsed three times with PBS. Cells were permeabilized with 0.1X triton for 12min at room temperature, then rinsed three times with PBS. Blocking was done in 3% BSA solution for 30min at room temperature. All incubations with primary antibodies were performed for either 1h at room temperature or overnight at 4°C with the following antibodies for H3K9me3 (Active Motif, 1:1000), DAXX (Santa Cruz, 1:500), H3K9me2 (Active Motif, 1:1000), LaminB1 (Abcam, 1:1000), PML (gift from Hugue de Thé, 1/2000) and SETDB1 (Proteintech, 1:100). Incubation with secondary antibodies (fluorescently labeled anti-mouse or anti-rabbit, 1:1000) were performed for 1h at room temperature. Mounting was performed using ProLong Diamond with DAPI mounting media (Thermo).

Fluorescent in situ Hybridization

Murine ES cells were harvested with trypsin (Gibco) and plated for 4-6h onto 0.1% gelatin-coated glass cover slips. Cells were fixed with 4% paraformaldehyde (PFA) for 10min at room temperature, then rinsed three times with PBS. Cells were permeabilized with 0.5X triton for 12min at room temperature, then rinsed three times with PBS. Cells were briefly washed in 2X SSC, then treated with RNAseA (100µg/mL, Sigma) for 1h at 37°C. Cells were briefly washed in 2X SSC, then denatured by serial 2min incubation into 70,90 and 100% ethanol. Cover slips were air dried for 15min. Cover slips are incubated with 200nM of PNA

probe, placed for 10min at 95°C for denaturation, then placed for 1h at room temperature in the dark for hybridization. Cover slips were washed twice in 2X SSC 0.1%Tween-20 for 10min at 60°C. Cover slips were immerged at room temperature in 2X SSC 0.1%Tween-20 for 2 min, then in 2X SSC for 2min and 1X SSC for 2min. Mounting is performed using ProLong Diamond with DAPI mounting media (Thermo).

Fluorescent Recovery After Photobleaching and variance analysis

Murine ES cells transfected with HP1α-GFP were harvested with trypsin (Gibco) and plated for 4-6h onto 0.1% gelatin-coated glass live-cell Nunc slides (Thermo). FRAP experiment was carried with an LSM 800 confocal microscope (Zeiss). The 488nm laser was used to bleach and acquire GFP signal. 1 image was taken before a bleach pulse of 5ms. Bleaching area was set to target a single pericentric domain. Images were acquired every second during 35s post-bleach. FRAP analysis was performed using a FRAP analysis ImageJ Jython script, that generated FRAP curves and the associated half-recovery time and mobile fraction parameters.

GFP-HP1α variance along time was obtained from ImageJ analysis using standard deviation z-projection along time for the whole duration of the movie. Quantification of heterochromatin barriers were performed using a 1µm line across individual non-bleached chromocenter borders, for which the variance intensity along time was measured with the ImageJ software.

Image acquisition and analysis

Images for immunofluorescence and FISH experiments were obtained with an inverted Nikon Ti Eclipse widefield microscope using a 60X immersion objective and LED sources. Z-stacks images were taken and then deconvoluted using a custom ImageJ deconvolution script. Quantifications of images were performed using custom Icy scripts in Icy and ImageJ. To quantify DAXX enrichment at PCH and the number of PCH foci, chromocenters were segmented using the spot detector function in ICY on either H3K9me3 or major satellite FISH signal. Nuclei were isolated using the ICY k-means segmentation script. The nuclear periphery enrichment was measured in ImageJ, briefly linescans of LaminB1 and H3K9me2 at the periphery were isolated using the straighten command and subsequently used to generated intensity profiles.

H3K9me3 intensities at chromocenters were measured using à 2µm line across individual DAPI-dense chromocenters. Two to three chromocenters per nucleus were analyzed.

Statistical analysis

Number of objects counted, and statistical tests performed are indicated in the text, figure or figure legends. All statistical analysis results are listed in supplementary file. Pvalues are represented as follow: * <0.05; **<0.01; ***<0.001; ****<0.0001. Statistical tests were performed using GraphPad Prism version 9.0.0. and R.

Western Blotting

Total protein extracts were prepared in RIPA buffer with protease inhibitor cocktail (Roche). Samples were sonicated for 3 minutes alterning 30seconds ON/ 30seconds OFF. Proteins were separated by electrophoresis in 8-15% poly-acrylamide gels then transferred onto nitrocellulose membranes. Membranes were incubated in ponceau then washed in PBS, 0.1% tween. Membranes were blocked in PBS, 0.1% tween, 5% milk for 30min at room temperature before incubation with primary antibody overnight at 4°C. After 3 washed in PBS, 0.1% tween, membranes were incubated with secondary HRP-conjugated antibody for 1h at room temperature. Membranes were washed 3 times in PBS, 0.1% tween and visualized by chemoluminescence using ECL Plus.

Acknowledgements

We would like to thank A. Bonnet-Garnier and A. Jouneau for the gift of Suv39dKO KO ESCs and advice. We are also grateful to image core microscopy facilities of IRSL, Paris, in particular N. Setterblad for his assistance with live imaging. We warmly thank V. Lallemand-Breitenbach and H. de Thé (Collège de France, Paris, France) for the sharing of PML antibody and helpful advice. We are thankful to Y. Khalil for her help in microscopy analysis. We kindly thank P. Lesage and Annia Carré Simon for their critical readings of the manuscript, and other members of the team for helpful advice. We finally thank support services of IRSL. This work was funded by Agence Nationale pour la Recherche (ANR-16-CE12-0003), IDEX SLI, La Ligue Nationale Contre le Cancer (LNCC)-Comité Ile de France and the labex Who am I. AC was supported by MESR and LNCC. The authors declare no conflict of interest.

Author Contributions

AC, AV, PT designed experiments. AC, AV, CD, PT, performed and analyzed experiments. PL, PAR generated the Tet1/2 DKO cell lines. FB performed LC-MS/MS analysis. RI analyzed RNAseq data. RB wrote the scripts for image analysis. EF, MVCG, PBA, PT acquired fundings. AC, EF, PT contributed to the writing of the manuscript. All authors reviewed the manuscript.

Funding

This work was supported by the Agence Nationale de la Recherche (grant number: ANR-16-CE12-0003-01) and Le comité Ile de France de La Ligue Contre le Cancer (grant number: RS22/75-43).

Data availability

Access to raw data for the RNA-Seq experiment is available from the Gene Expression Omnibus (GEO) under accession number GSE000000. Original microscopy data are available upon request.

Declaration of interest

The authors declare no competing interests.

References

Adam, S., Polo, S. E. and Almouzni, G. (2013). Transcription recovery after DNA damage requires chromatin priming by the H3.3 histone chaperone HIRA. *Cell* **155**, 94–106.

Aloia, L., Stefano, B. D. and Croce, L. D. (2013). Polycomb complexes in stem cells and embryonic development. *Development* **140**, 2525–2534.

Arakawa, T., Nakatani, T., Oda, M., Kimura, Y., Sekita, Y., Kimura, T., Nakamura, T. and Nakano, T. (2015). Stella controls chromocenter formation through regulation of Daxx expression in 2-cell embryos. *Biochemical and biophysical research communications* **466**, 60–65.

Bannister, A. J., Zegerman, P., Partridge, J. F., Miska, E. A., Thomas, J. O., Allshire, R. C. and Kouzarides, T. (2001). Selective recognition of methylated lysine 9 on histone H3 by the HP1 chromo domain. *Nature* **410**, 120–4.

Blaschke, K., Ebata, K. T., Karimi, M. M., Zepeda-Martínez, J. A., Goyal, P., Mahapatra, S., Tam, A., Laird, D. J., Hirst, M., Rao, A., et al. (2013). Vitamin C induces Tet-dependent DNA demethylation and a blastocyst-like state in ES cells. *Nature* **500**, 222–226.

Borgel, J., Guibert, S., Li, Y., Chiba, H., Schübeler, D., Sasaki, H., Forné, T. and Weber, M. (2010). Targets and dynamics of promoter DNA methylation during early mouse development. *Nature Genetics* **42**, 1093–1100.

Burton, A. and Torres-Padilla, M.-E. (2014). Chromatin dynamics in the regulation of cell fate allocation during early embryogenesis. *Nat Rev Mol Cell Bio* **15**, 723–735.

Buschbeck, M. and Hake, S. B. (2017). Variants of core histones and their roles in cell fate decisions, development and cancer. *Nature Reviews Molecular Cell Biology* **18**, 299–314.

Carraro, M., Hendriks, I. A., Hammond, C. M., Solis-Mezarino, V., Völker-Albert, M., Elsborg, J. D., Weisser, M. B., Spanos, C., Montoya, G., Rappsilber, J., et al. (2023). DAXX adds a de novo H3.3K9me3 deposition pathway to the histone chaperone network. *Mol Cell* **83**, 1075-1092.e9.

Casanova, M., Pasternak, M., Marjou, F. E., Baccon, P. L., Probst, A. V. and Almouzni, G. (2013). Heterochromatin reorganization during early mouse development requires a single-stranded noncoding transcript. *Cell reports* **4**, 1156–1167.

Cho, S., Park, J. S. and Kang, Y.-K. (2011). Dual functions of histone-lysine N-methyltransferase Setdb1 protein at promyelocytic leukemia-nuclear body (PML-NB): maintaining PML-NB structure and regulating the expression of its associated genes. *Journal of Biological Chemistry* **286**, 41115–41124.

Cho, S., Park, J. S., Kwon, S. and Kang, Y.-K. (2012). Dynamics of Setdb1 expression in early mouse development. *Gene expression patterns : GEP* **12**, 213–218.

Consortium, M. G. S., Waterston, R. H., Lindblad-Toh, K., Birney, E., Rogers, J., Abril, J. F., Agarwal, P., Agarwala, R., Ainscough, R., Alexandersson, M., et al. (2002). Initial sequencing and comparative analysis of the mouse genome. *Nature* **420**, 520–562.

Crosetto, N., Mitra, A., Silva, M. J., Bienko, M., Dojer, N., Wang, Q., Karaca, E., Chiarle, R., Skrzypczak, M., Ginalski, K., et al. (2013). Nucleotide-resolution DNA double-strand break mapping by next-generation sequencing. *Nature methods* **10**, 361–365.

Delbarre, E., Ivanauskiene, K., Küntziger, T. and Collas, P. (2013). DAXX-dependent supply of soluble (H3.3-H4) dimers to PML bodies pending deposition into chromatin. *Genome Research* **23**, 440–451.

Delbarre, E., Ivanauskiene, K., Spirkoski, J., Shah, A., Vekterud, K., Moskaug, J. Ø., Bøe, S. O., Wong, L. H., Küntziger, T. and Collas, P. (2017). PML protein organizes heterochromatin domains where it regulates histone H3.3 deposition by ATRX/DAXX. *Genome Research* **27**, 913–921.

Ding, Q., Lee, Y.-K., Schaefer, E. A. K., Peters, D. T., Veres, A., Kim, K., Kuperwasser, N., Motola, D. L., Meissner, T. B., Hendriks, W. T., et al. (2013). A TALEN genome-editing system for generating human stem cell-based disease models. *Cell stem cell* **12**, 238–251.

Drané, P., Ouararhni, K., Depaux, A., Shuaib, M. and Hamiche, A. (2010). The death-associated protein DAXX is a novel histone chaperone involved in the replication-independent deposition of H3.3. *Genes & Development* **24**, 1253–1265.

Dubois, A., Vincenti, L., Chervova, A., Greenberg, M. V. C., Vandormael-Pournin, S., Bourc'his, D., Cohen-Tannoudji, M. and Navarro, P. (2022). H3K9 tri-methylation at Nanog times differentiation commitment and enables the acquisition of primitive endoderm fate. *Dev Camb Engl* **149**, dev201074.

Elsässer, S. J., Huang, H., Lewis, P. W., Chin, J. W., Allis, C. D. and Patel, D. J. (2012). DAXX envelops a histone H3.3-H4 dimer for H3.3-specific recognition. *Nature* **491**, 560–565.

Elsässer, S. J., Noh, K.-M., Diaz, N., Allis, C. D. and Banaszynski, L. A. (2015). Histone H3.3 is required for endogenous retroviral element silencing in embryonic stem cells. *Nature* **522**, 240–244.

Escobar-Cabrera, E., Lau, D. K. W., Giovinazzi, S., Ishov, A. M. and McIntosh, L. P. (2010). Structural characterization of the DAXX N-terminal helical bundle domain and its complex with Rassf1C. *Structure (London, England : 1993)* **18**, 1642–1653.

Falk, M., Feodorova, Y., Naumova, N., Imakaev, M., Lajoie, B. R., Leonhardt, H., Joffe, B., Dekker, J., Fudenberg, G., Solovei, I., et al. (2019). Heterochromatin drives compartmentalization of inverted and conventional nuclei. *Nature* **40**, 47.

Fortuny, A., Chansard, A., Caron, P., Chevallier, O., Leroy, O., Renaud, O. and Polo, S. E. (2021). Imaging the response to DNA damage in heterochromatin domains reveals core principles of heterochromatin maintenance. *Nature communications* **12**, 2428–16.

Fukuda, K., Okuda, A., Yusa, K. and Shinkai, Y. (2018). A CRISPR knockout screen identifies SETDB1-target retroelement silencing factors in embryonic stem cells. *Genome Research* **28**, 846–858.

Gauchier, M., Kan, S., Barral, A., Sauzet, S., Agirre, E., Bonnell, E., Saksouk, N., Barth, T. K., Ide, S., Urbach, S., et al. (2019). SETDB1-dependent heterochromatin stimulates alternative lengthening of telomeres. *Science advances* **5**, eaav3673.

Guelen, L., Pagie, L., Brasset, E., Meuleman, W., Faza, M. B., Talhout, W., Eussen, B. H., Klein, A. de, Wessels, L., Laat, W. de, et al. (2008). Domain organization of human chromosomes revealed by mapping of nuclear lamina interactions. *Nature* **453**, 948–951.

Guenatri, M., Bailly, D., Maison, C. and Almouzni, G. (2004). Mouse centric and pericentric satellite repeats form distinct functional heterochromatin. *The Journal of cell biology* **166**, 493–505.

Hahn, M., Dambacher, S., Dulev, S., Kuznetsova, A. Y., Eck, S., Wörz, S., Sadic, D., Schulte, M., Mallm, J.-P., Maiser, A., et al. (2013). Suv4-20h2 mediates chromatin compaction and is important for cohesin recruitment to heterochromatin. *Genes & Development* **27**, 859–872.

He, Q., Kim, H., Huang, R., Lu, W., Tang, M., Shi, F., Yang, D., Zhang, X., Huang, J., Liu, D., et al. (2015). The Daxx/Atrx Complex Protects Tandem Repetitive Elements during DNA Hypomethylation by Promoting H3K9 Trimethylation. *Cell stem cell* **17**, 273–286.

Healton, S. E., Pinto, H. D., Mishra, L. N., Hamilton, G. A., Wheat, J. C., Swist-Rosowska, K., Shukeir, N., Dou, Y., Steidl, U., Jenuwein, T., et al. (2020). H1 linker histones silence repetitive elements by promoting both histone H3K9 methylation and chromatin compaction. *Proceedings of the National Academy of Sciences of the United States of America* **117**, 14251–14258.

Henderson, A., Wu, Y., Huang, Y. C., Chavez, E. A., Platt, J., Johnson, F. B., Brosh, R. M., Sen, D. and Lansdorp, P. M. (2017). Detection of G-quadruplex DNA in mammalian cells. *Nucleic Acids Res.* **45**, 6252–6252.

Hinde, E., Cardarelli, F. and Gratton, E. (2015). Spatiotemporal regulation of Heterochromatin Protein 1-alpha oligomerization and dynamics in live cells. *Scientific reports* **5**, 12001–11.

Hoelper, D., Huang, H., Jain, A. Y., Patel, D. J. and Lewis, P. W. (2017). Structural and mechanistic insights into ATRX-dependent and -independent functions of the histone chaperone DAXX. *Nature communications* **8**, 1193.

Jachowicz, J. W., Bing, X., Pontabry, J., Bošković, A., Rando, O. J. and Torres-Padilla, M.-E. (2017). LINE-1 activation after fertilization regulates global chromatin accessibility in the early mouse embryo. *Nature Genetics* **11**, 778.

Jagannathan, M., Cummings, R. and Yamashita, Y. M. (2018). A conserved function for pericentromeric satellite DNA. *eLife* **7**, 1218.

Jang, C.-W., Shibata, Y., Starmer, J., Yee, D. and Magnuson, T. (2015). Histone H3.3 maintains genome integrity during mammalian development. *Genes & Development* **29**, 1377–1392.

Juhász, S., Elbakry, A., Mathes, A. and Löbrich, M. (2018). ATRX Promotes DNA Repair Synthesis and Sister Chromatid Exchange during Homologous Recombination. *Molecular Cell* **71**, 11-24.e7.

Jurkowska, R. Z., Qin, S., Kungulovski, G., Tempel, W., Liu, Y., Bashtrykov, P., Stiefelmaier, J., Jurkowski, T. P., Kudithipudi, S., Weirich, S., et al. (2017). H3K14ac is linked to methylation of H3K9 by the triple Tudor domain of SETDB1. *Nature communications* **8**, 2057.

Karimi, M. M., Goyal, P., Maksakova, I. A., Bilenky, M., Leung, D., Tang, J. X., Shinkai, Y., Mager, D. L., Jones, S., Hirst, M., et al. (2011). DNA methylation and SETDB1/H3K9me3 regulate predominantly distinct sets of genes, retroelements, and chimeric transcripts in mESCs. **8**, 676–687.

Kind, J., Pagie, L., Ortabozkoyun, H., Boyle, S., Vries, S. S. de, Janssen, H., Amendola, M., Nolen, L. D., Bickmore, W. A. and Steensel, B. van (2013). Single-cell dynamics of genome-nuclear lamina interactions. *Cell* **153**, 178–192.

Koningsbruggen, S. van, Gierlinski, M., Schofield, P., Martin, D., Barton, G. J., Ariyurek, Y., Dunnen, J. T. den and Lamond, A. I. (2010). High-resolution whole-genome sequencing reveals that specific chromatin domains from most human chromosomes associate with nucleoli. *Molecular biology of the cell* **21**, 3735–3748.

Lachner, M., O'Carroll, D., Rea, S., Mechtler, K. and Jenuwein, T. (2001). Methylation of histone H3 lysine 9 creates a binding site for HP1 proteins. *Nature* **410**, 116–120.

Lallemand-Breitenbach, V. and Thé, H. de (2018). PML nuclear bodies: from architecture to function. *Current Opinion in Cell Biology* **52**, 154–161.

Larson, A. G., Elnatan, D., Keenen, M. M., Trnka, M. J., Johnston, J. B., Burlingame, A. L., Agard, D. A., Redding, S. and Narlikar, G. J. (2017). Liquid droplet formation by HP1α suggests a role for phase separation in heterochromatin. *Nature* **547**, 236–240.

Lehnertz, B., Ueda, Y., Derijck, A. A. H. A., Braunschweig, U., Perez-Burgos, L., Kubicek, S., Chen, T., Li, E., Jenuwein, T. and Peters, A. H. F. M. (2003). Suv39h-mediated histone H3 lysine 9 methylation directs DNA methylation to major satellite repeats at pericentric heterochromatin. *Current Biology* **13**, 1192–1200.

Leitch, H. G., McEwen, K. R., Turp, A., Encheva, V., Carroll, T., Grabole, N., Mansfield, W., Nashun, B., Knezovich, J. G., Smith, A., et al. (2013). Naive pluripotency is associated with global DNA hypomethylation. *Nature structural & molecular biology* **20**, 1–9.

Lewis, P. W., Elsaesser, S. J., Noh, K.-M., Stadler, S. C. and Allis, C. D. (2010). Daxx is an H3.3-specific histone chaperone and cooperates with ATRX in replication-independent chromatin assembly at telomeres. *Proceedings of the National Academy of Sciences of the United States of America* **107**, 14075–14080.

Li, X. and Tyler, J. K. (2016). Nucleosome disassembly during human non-homologous end joining followed by concerted HIRA- and CAF-1-dependent reassembly. *eLife* **5**, 94.

Lin, C.-J., Conti, M. and Ramalho-Santos, M. (2013). Histone variant H3.3 maintains a decondensed chromatin state essential for mouse preimplantation development. *Development* **140**, 3624–3634.

Liu, Z., Tardat, M., Gill, M. E., Royo, H., Thierry, R., Ozonov, E. A. and Peters, A. H. (2020). SUMOylated PRC1 controls histone H3.3 deposition and genome integrity of embryonic heterochromatin. *The EMBO Journal* e103697.

Loyola, A., Tagami, H., Bonaldi, T., Roche, D., Quivy, J.-P., Imhof, A., Nakatani, Y., Dent, S. Y. R. and Almouzni, G. (2009). The HP1alpha-CAF1-SetDB1-containing complex provides H3K9me1 for Suv39-mediated K9me3 in pericentric heterochromatin. *EMBO reports* **10**, 769–775.

Lu, J. Y., Chang, L., Li, T., Wang, T., Yin, Y., Zhan, G., Han, X., Zhang, K., Tao, Y., Percharde, M., et al. (2021). Homotypic clustering of L1 and B1/Alu repeats compartmentalizes the 3D genome. *Cell research* **1**, 26.

Luciani, J. J., Depetris, D., Usson, Y., Metzler-Guillemain, C., Mignon-Ravix, C., Mitchell, M. J., Megarbane, A., Sarda, P., Sirma, H., Moncla, A., et al. (2006). PML nuclear bodies are highly organised DNA-protein structures with a function in heterochromatin remodelling at the G2 phase. *Journal of Cell Science* **119**, 2518–2531.

Luijsterburg, M. S., Krijger, I. de, Wiegant, W. W., Shah, R. G., Smeenk, G., Groot, A. J. L. de, Pines, A., Vertegaal, A. C. O., Jacobs, J. J. L., Shah, G. M., et al. (2016). PARP1 Links CHD2-Mediated Chromatin Expansion and H3.3 Deposition to DNA Repair by Non-homologous End-Joining. *Molecular Cell* **61**, 547–562.

Mansuroglu, Z., Benhelli-Mokrani, H., Marcato, V., Sultan, A., Violet, M., Chauderlier, A., Delattre, L., Loyens, A., Talahari, S., Bégard, S., et al. (2016). Loss of Tau protein affects the structure, transcription and repair of neuronal pericentromeric heterochromatin. *Scientific reports* **6**, 33047.

Martens, J. H. A., O'Sullivan, R. J., Braunschweig, U., Opravil, S., Radolf, M., Steinlein, P. and Jenuwein, T. (2005). The profile of repeat-associated histone lysine methylation states in the mouse epigenome. *The EMBO Journal* **24**, 800–812.

Matsui, T., Leung, D., Miyashita, H., Maksakova, I. A., Miyachi, H., Kimura, H., Tachibana, M., Lorincz, M. C. and Shinkai, Y. (2010). Proviral silencing in embryonic stem cells requires the histone methyltransferase ESET. *Nature* **464**, 927–931.

Mattout, A., Aaronson, Y., Sailaja, B. S., Ram, E. V. R., Harikumar, A., Mallm, J.-P., Sim, K. H., Nissim-Rafinia, M., Supper, E., Singh, P. B., et al. (2015). Heterochromatin Protein 1β (HP1β) has distinct functions and distinct nuclear distribution in pluripotent versus differentiated cells. *Genome Biol.* **16**, 213.

Mendiratta, S., Gatto, A. and Almouzni, G. (2019). Histone supply: Multitiered regulation ensures chromatin dynamics throughout the cell cycle. *J Cell Biol* **218**, 39–54.

Michaelson, J. S., Bader, D., Kuo, F., Kozak, C. and Leder, P. (1999). Loss of Daxx, a promiscuously interacting protein, results in extensive apoptosis in early mouse development. *Genes & Development* **13**, 1918–1923.

Miyanari, Y., Ziegler-Birling, C. and Torres-Padilla, M.-E. (2013). Live visualization of chromatin dynamics with fluorescent TALEs. *Nat Biotechnology* **20**, 1321–1324.

Mulholland, C. B., Traube, F. R., Ugur, E., Parsa, E., Eckl, E.-M., Schönung, M., Modic, M., Bartoschek, M. D., Stolz, P., Ryan, J., et al. (2020). Distinct and stage-specific contributions of TET1 and TET2 to stepwise cytosine oxidation in the transition from naive to primed pluripotency. *Sci. Rep.* **10**, 12066.

Nakatani, T., Yamagata, K., Kimura, T., Oda, M., Nakashima, H., Hori, M., Sekita, Y., Arakawa, T., Nakamura, T. and Nakano, T. (2015). Stella preserves maternal chromosome integrity by inhibiting 5hmC-induced γH2AX accumulation. *EMBO reports* **16**, 582–589.

Pailles, M., Hirlemann, M., Brochard, V., Chebrout, M., Oudin, J.-F., Marks, H., Jouneau, A. and Bonnet-Garnier, A. (2022). H3K27me3 at pericentromeric heterochromatin is a defining feature of the early mouse blastocyst. *Sci Rep-uk* **12**, 13908.

Park, J., Lee, H., Han, N., Kwak, S., Lee, H.-T., Kim, J.-H., Kang, K., Youn, B. H., Yang, J.-H., Jeong, H.-J., et al. (2018). Long non-coding RNA ChRO1 facilitates ATRX/DAXX-dependent H3.3 deposition for transcription-associated heterochromatin reorganization. *Nucleic acids research* **46**, 11759–11775.

Peric-Hupkes, D., Meuleman, W., Pagie, L., Bruggeman, S. W. M., Solovei, I., Brugman, W., Gräf, S., Flicek, P., Kerkhoven, R. M., Lohuizen, M. van, et al. (2010). Molecular maps of the reorganization of genome-nuclear lamina interactions during differentiation. *Molecular Cell* **38**, 603–613.

Peters, A. H., O'Carroll, D., Scherthan, H., Mechtler, K., Sauer, S., Schöfer, C., Weipoltshammer, K., Pagani, M., Lachner, M., Kohlmaier, A., et al. (2001). Loss of the Suv39h histone methyltransferases impairs mammalian heterochromatin and genome stability. *Cell* **107**, 323–337.

Pinheiro, I., Margueron, R., Shukeir, N., Eisold, M., Fritzsch, C., Richter, F. M., Mittler, G., Genoud, C., Goyama, S., Kurokawa, M., et al. (2012). Prdm3 and Prdm16 are H3K9me1 methyltransferases required for mammalian heterochromatin integrity. *Cell* **150**, 948–960.

Probst, A. V., Okamoto, I., Casanova, M., Marjou, F. E., Baccon, P. L. and Almouzni, G. (2010). A strand-specific burst in transcription of pericentric satellites is required for chromocenter formation and early mouse development. *Developmental Cell* **19**, 625–638.

Sadic, D., Schmidt, K., Groh, S., Kondofersky, I., Ellwart, J., Fuchs, C., Theis, F. J. and Schotta, G. (2015). Atrx promotes heterochromatin formation at retrotransposons. *EMBO reports* **16**, 836–850.

Saksouk, N., Barth, T. K., Ziegler-Birling, C., Olova, N., Nowak, A., Rey, E., Mateos-Langerak, J., Urbach, S., Reik, W., Torres-Padilla, M.-E., et al. (2014). Redundant mechanisms to form silent chromatin at pericentromeric regions rely on BEND3 and DNA methylation. *Molecular Cell* **56**, 580–594.

Salsman, J., Rapkin, L. M., Margam, N. N., Duncan, R., Bazett-Jones, D. P. and Dellaire, G. (2017). Myogenic differentiation triggers PML nuclear body loss and DAXX relocalization to chromocentres. *Cell death & disease* **8**, e2724.

Song, Y. J., Choi, J. H. and Lee, H. (2015). Setdb1 is required for myogenic differentiation of C2C12 myoblast cells via maintenance of MyoD expression. *Molecules and cells* **38**, 362–372.

Strom, A. R., Emelyanov, A. V., Mir, M., Fyodorov, D. V., Darzacq, X. and Karpen, G. H. (2017). Phase separation drives heterochromatin domain formation. *Nature* **547**, 241–245.

Szenker, E., Ray-Gallet, D. and Almouzni, G. (2011). The double face of the histone variant H3.3. *Cell research* **21**, 421–434.

Teng, Y.-C., Sundaresan, A., O'Hara, R., Gant, V. U., Li, M., Martire, S., Warshaw, J. N., Basu, A. and Banaszynski, L. A. (2021). ATRX promotes heterochromatin formation to protect cells from G-quadruplex DNA-mediated stress. *Nat Commun* **12**, 3887.

Tessier, S., Ferhi, O., Geoffroy, M.-C., González-Prieto, R., Canat, A., Quentin, S., Pla, M., Niwa-Kawakita, M., Bercier, P., Rérolle, D., et al. (2022). Exploration of nuclear body-enhanced sumoylation reveals that PML represses 2-cell features of embryonic stem cells. *Nat Commun* **13**, 5726.

Therizols, P., Illingworth, R. S., Courilleau, C., Boyle, S., Wood, A. J. and Bickmore, W. A. (2014). Chromatin decondensation is sufficient to alter nuclear organization in embryonic stem cells. *Science* **346**, 1238–1242.

Tosolini, M., Brochard, V., Adenot, P., Chebrout, M., Grillo, G., Navia, V., Beaujean, N., Francastel, C., Bonnet-Garnier, A. and Jouneau, A. (2018). Contrasting epigenetic states of heterochromatin in the different types of mouse pluripotent stem cells. *Scientific reports* **8**, 5776.

Udugama, M., Chang, F. T. M., Chan, F. L., Tang, M. C., Pickett, H. A., McGhie, J. D. R., Mayne, L., Collas, P., Mann, J. R. and Wong, L. H. (2015). Histone variant H3.3 provides the heterochromatic H3 lysine 9 tri-methylation mark at telomeres. *Nucleic acids Res.* **43**, 10227–37.

Walter, M., Teissandier, A., Pérez-Palacios, R. and Bourc'his, D. (2016). An epigenetic switch ensures transposon repression upon dynamic loss of DNA methylation in embryonic stem cells. *eLife* **5**, R87.

Wang, L., Gao, Y., Zheng, X., Liu, C., Dong, S., Li, R., Zhang, G., Wei, Y., Qu, H., Li, Y., et al. (2019). Histone Modifications Regulate Chromatin Compartmentalization by Contributing to a Phase Separation Mechanism. *Molecular Cell* **76**, 646-659.e6.

Wijchers, P. J., Geeven, G., Eyres, M., Bergsma, A. J., Janssen, M., Verstegen, M., Zhu, Y., Schell, Y., Vermeulen, C., Wit, E. de, et al. (2015). Characterization and dynamics of pericentromere-associated domains in mice. *Genome Research* **25**, 958–969.

Wossidlo, M., Nakamura, T., Lepikhov, K., Marques, C. J., Zakhartchenko, V., Boiani, M., Arand, J., Nakano, T., Reik, W. and Walter, J. (2011). 5-Hydroxymethylcytosine in the mammalian zygote is linked with epigenetic reprogramming. *Nature communications* **2**, 241.

Ying, Q.-L., Wray, J., Nichols, J., Batlle-Morera, L., Doble, B., Woodgett, J., Cohen, P. and Smith, A. (2008). The ground state of embryonic stem cell self-renewal. *Nature* **453**, 519–523.

Zhu, Q., Pao, G. M., Huynh, A. M., Suh, H., Tonnu, N., Nederlof, P. M., Gage, F. H. and Verma, I. M. (2011). BRCA1 tumour suppression occurs via heterochromatin-mediated silencing. *Nature* **477**, 179–184.

Ziegler-Birling, C., Helmrich, A., Tora, L. and Torres-Padilla, M.-E. (2009). Distribution of p53 binding protein 1 (53BP1) and phosphorylated H2A.X during mouse preimplantation development in the absence of DNA damage. *The International journal of developmental biology* **53**, 1003–1011.

Figures

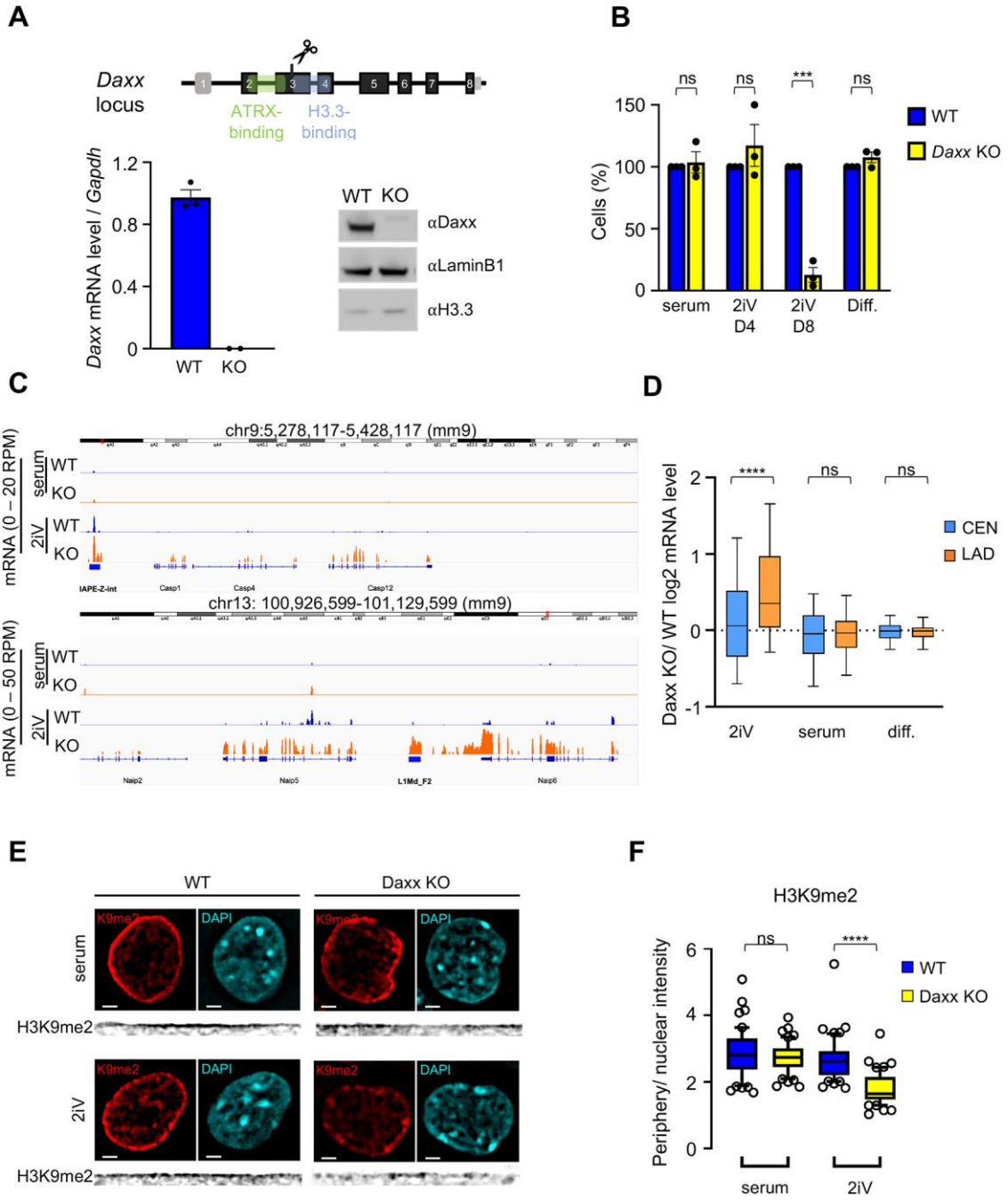

Fig. 1. DAXX is essential for ESC survival upon ground-state conversion and is required for transcriptional repression of peripheral heterochromatin. (A) Schematic of the *Daxx* locus and the of the guide RNA targeting exon 3. Left, RT-qPCR experiment on DAXX RNA in WT cells or cells after CrispR/cas9 editing on *Daxx*. The mean of two biological replicates with SEM are shown. Right, western blot with anti-DAXX antibody, anti-LAMIN-B1 and anti-H3.3 served as loading control. One experiment from at least 2 biological

replicates is shown. **(B)** Quantification of the number of cells (in %) compared to WT in each culture condition, serum, after 4 days (4d) or 8 days (8d) of 2iV conversion and after 5 days of Retinoic Acid differentiation (Diff.) Bar plots represents mean of 3 biological replicates for each condition. Error bars represent s.e.m. T-tests were used for statistical analysis. ns, not significant; ***P<0.001. **(C)** RNA-seq tracks of 2 Lamin Associated Domains (LAD) of WT ESCs (blue) and *Daxx* KO (orange) under serum and 2iV conditions. **(D)** Boxplots of the log2 fold change of mRNA levels of genes located in LAD (LAD, orange) and non-LAD (CEN, blue) regions in *Daxx* KO over WT ESCs, grown in 2iV, serum and diff. media. Two-sided Mann-Whitney tests were used for statistical analysis. ns, not significant; ****P<0.0001. **(E)** Representative nuclei after immuno-detection of H3K9me2 (red) and counterstaining with DAPI (blue) in WT and *Daxx* KO ESCs in serum and 2iV (scale bar = 2µm). Linescans below represent straighten H3K9me2 signal at the nuclear periphery (black). **(F)** Boxplots of H3K9me2 signal quantification enrichment at the nuclear periphery from 2 independent replicates. Two-sided Mann-Whitney tests were used for statistical analysis. ns, not significant; ****P<0.0001.

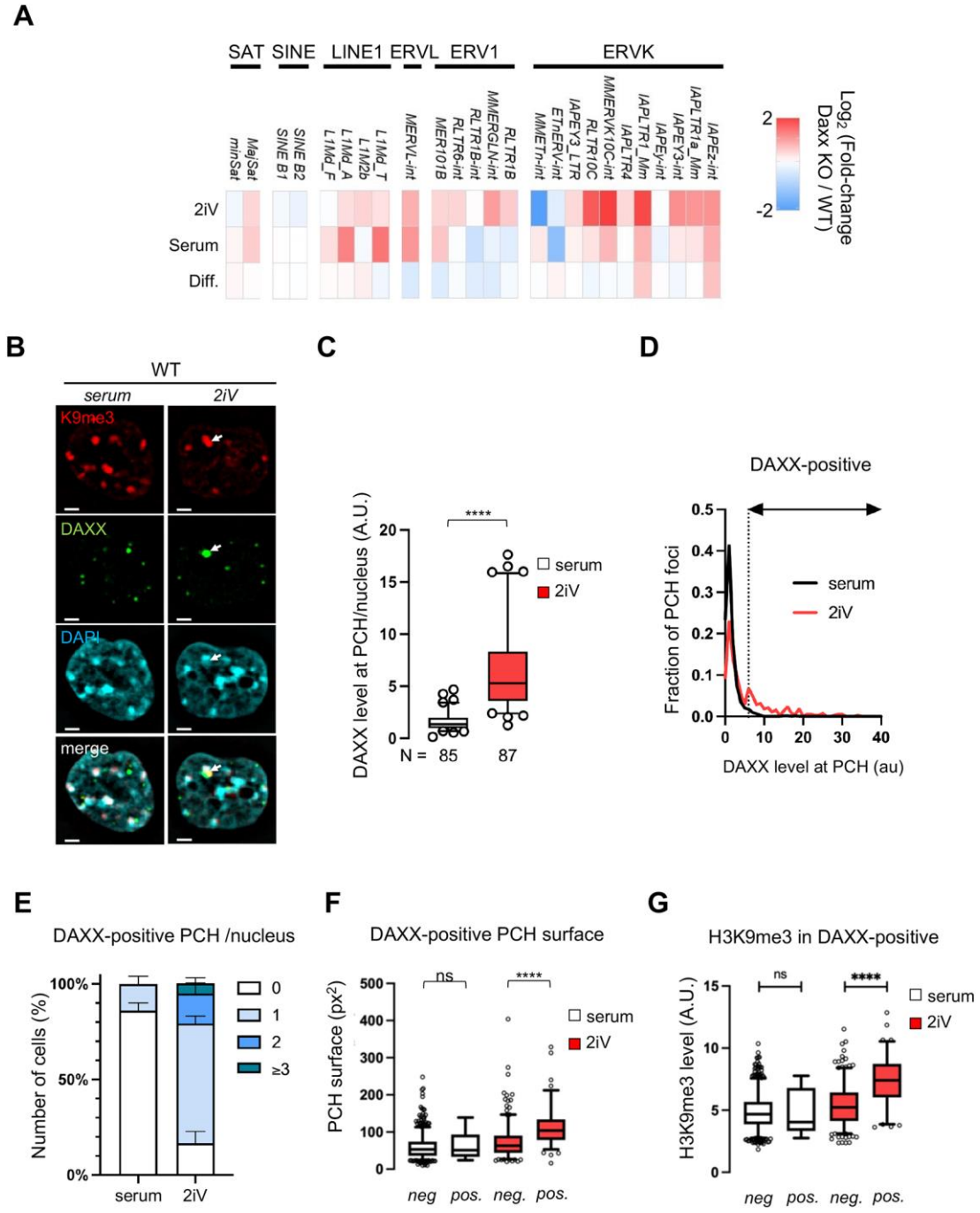

Fig. 2. DAXX is recruited to PCH in 2iV converted ESCs. (A) Heatmap for different classes of transposable elements. Data are mean from RNA-seq experiments on 3 biological replicates. **(B)** Representative nuclei of ESCs grown in serum or 2iV immuno-detected with H3K9me3 (red) and DAXX (green). Nuclei were counterstained with DAPI (cyan). Scale bar = 2µm. **(C)** Boxplot of mean DAXX levels at pericentromeric heterochromatin (PCH) in WT ESCs grown in serum (white) or in 2iV (red) from 3 biological replicates. Two-sided Mann-Whitney tests was used for statistical analysis. ****P<0.0001. **(D)** Distribution of DAXX intensity observed at individual PCH foci in WT ESCs grown in serum (black) or in 2iV (red)

from 3 independent replicates. Dashed line indicates the threshold used to defined DAXX-positive PCH. **(E)** Stacked bar plots of the average fraction of the cell population with 0, 1, 2 and 3 or more, DAXX-positive PCH foci in WT ESCs in serum and 2iV. Error bars represent s.e.m. **(F)** Boxplot of PCH foci surface based on their colocalization with DAXX (pos) or the absence of DAXX (neg) in WT ESCs grown in serum (white) or in 2iV (red). Two-sided Mann-Whitney tests were used for statistical analysis. ns, not significant; ****P<0.0001. **(G)** Boxplot of H3K9me3 intensity at PCH foci based on their colocalization with DAXX (pos) or the absence of DAXX (neg) in WT ESCs grown in serum (white) or in 2iV (red). in WT ESCs grown in serum (white) or in 2iV (red). Two-sided Mann-Whitney tests were used for statistical analysis. ns, not significant; ****P<0.0001.

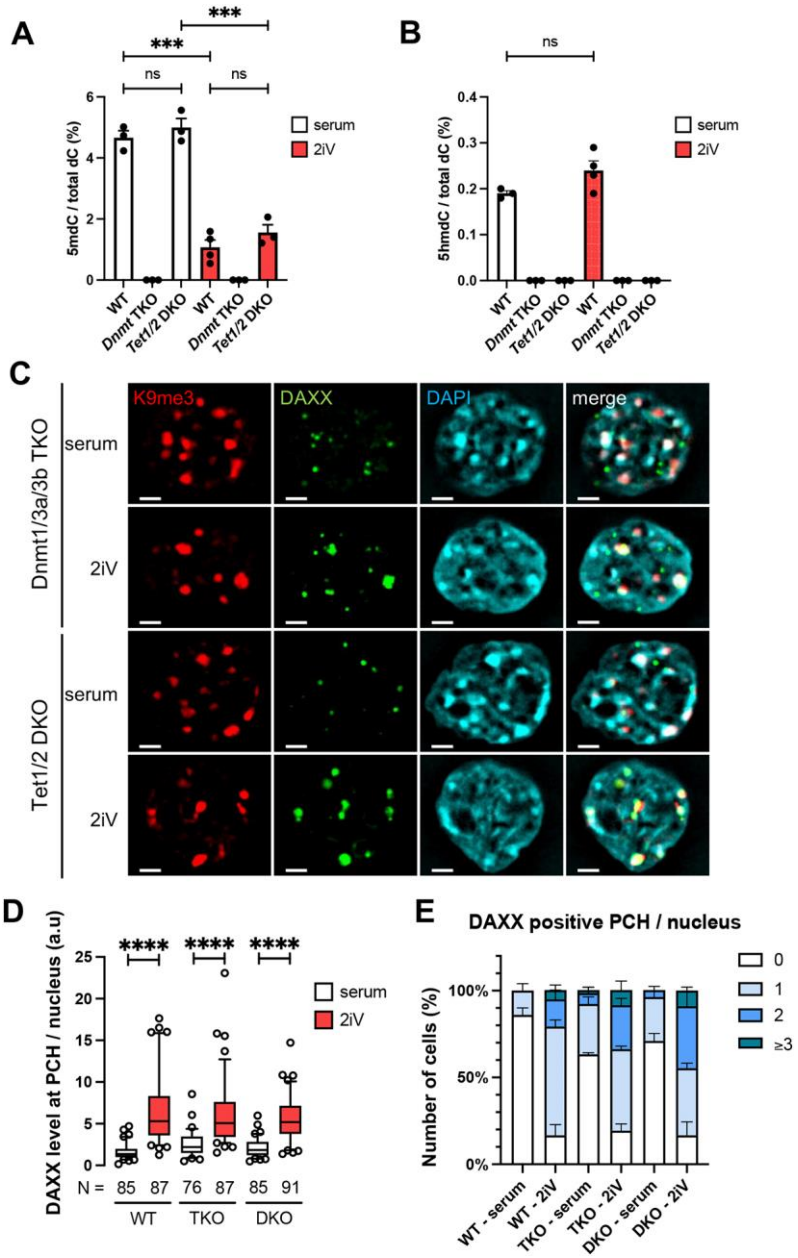

Fig. 3. DAXX Recruitment to PCH is Unaffected by the DNA Methylation Cycle. (A) Quantitation of 5-mC abundance in the cells by LC-MS/MS. Error bars represent s.e.m. T-tests were used for statistical analysis. ns, not significant; ***P<0.001. **(B)** Quantitation of 5-hmC abundance in the cells by LC-MS/MS. Error bars represent s.e.m. T-tests was used for statistical analysis. ns, not significant. **(C)** Representative nuclei of *Tet1/2* DKO and *Dnmt* TKO ESCs grown in serum or 2iV immuno-detected with H3K9me3 (red) and DAXX (green). Nuclei were counterstained with DAPI (cyan). Scale bar = 2µm. **(D)** Boxplot of mean DAXX levels at pericentromeric heterochromatin (PCH) in WT, *Tet1/2* DKO and *Dnmt* TKO ESCs

grown in serum (white) or in 2iV (red) from 3 biological replicates. WT values are taken from Fig. 2C. Two-sided Mann-Whitney tests were used for statistical analysis. ****P<0.0001. **(E)** Stacked bar plots of the average fraction of the cell population with 0, 1, 2 and 3 or more, DAXX-positive PCH foci in WT ESCs in serum and 2iV. SEM are shown. WT values are taken from Fig. 2E.

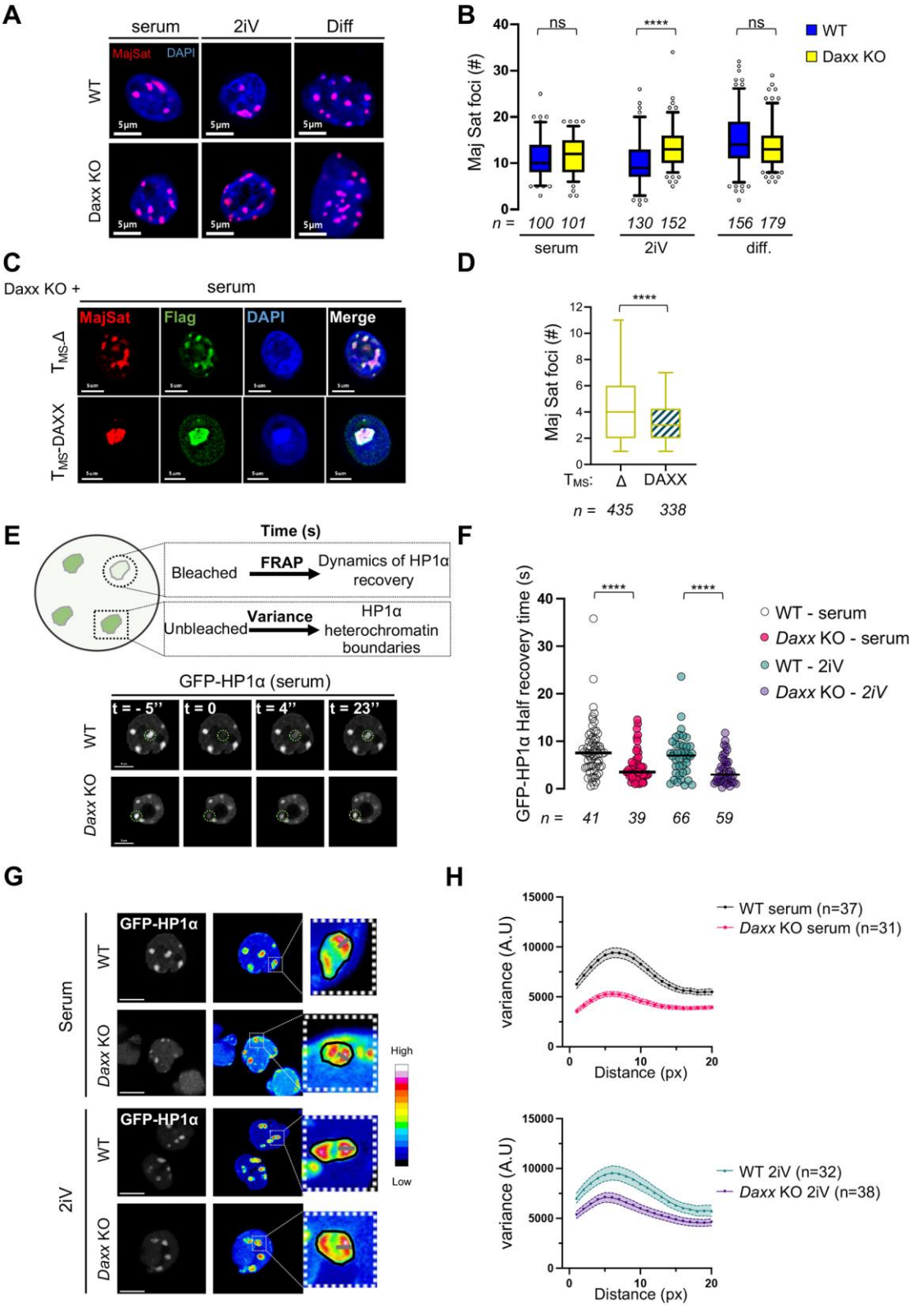

Fig. 4. DAXX maintains heterochromatin organization in pluripotent cells. (A) Representative major satellite (MajSat) DNA FISH pictures of WT and Daxx KO ESCs in serum, 2iV and differentiation (Diff.) conditions. **(B)** Quantification of the number of major

satellite foci per nucleus in WT (blue) or *Daxx* KO (yellow) ESC. n=total number of nuclei analyzed from at least 3 biological replicates. Two-sided Mann-Whitney tests were used for statistical analysis. ns, not significant; ****P<0.0001. **(C)** Representative immunoFISH pictures of major satellite and Flag for *Daxx* KO cells transfected with $TALE_{MajSat}$-Δ or $TALE_{MajSat}$-DAXX. **(D)** Quantification of the number of major satellite foci detected in the focal plane. n= total number of nuclei analyzed from 4 biological replicates. Two-sided Mann-Whitney tests was used for statistical analysis. ****P<0.0001. **(E)** Top, scheme depicting the two different analyses used in live-imaging experiments. Bottom, representative pictures from FRAP experiments performed on WT and *Daxx* KO cells transfected with GFP-HP1α. t=-5'' corresponds to pre-bleach fluorescence. t=0 corresponds to the laser bleach pulse. t=4'' and t=23'' correspond to post-bleach recovery images after 4 and 23 seconds respectively. **(F)** Quantification of half-recovery times in seconds for individual nuclei. n=total number of nuclei analyzed from 2 biological replicates. Two-sided Mann-Whitney tests were used for statistical analysis. ****P<0.0001. **(G)** Microscopy images displaying GFP-HP1α and the corresponding variance in fluorescence intensities over time in both serum and 2iV conditions, in WT and Daxx KO ESCs. The regions within the white dashed squares highlight individual chromocenters, further magnified in adjacent images for detailed view. Black lines delineate the border of chromocenters. Color correspondence of signal variance strength (from high to low) is shown. Scale bar, 5µm. **(H)** Graph displaying the variance intensities along measured on 1µm lines traced above non-bleached PCH.

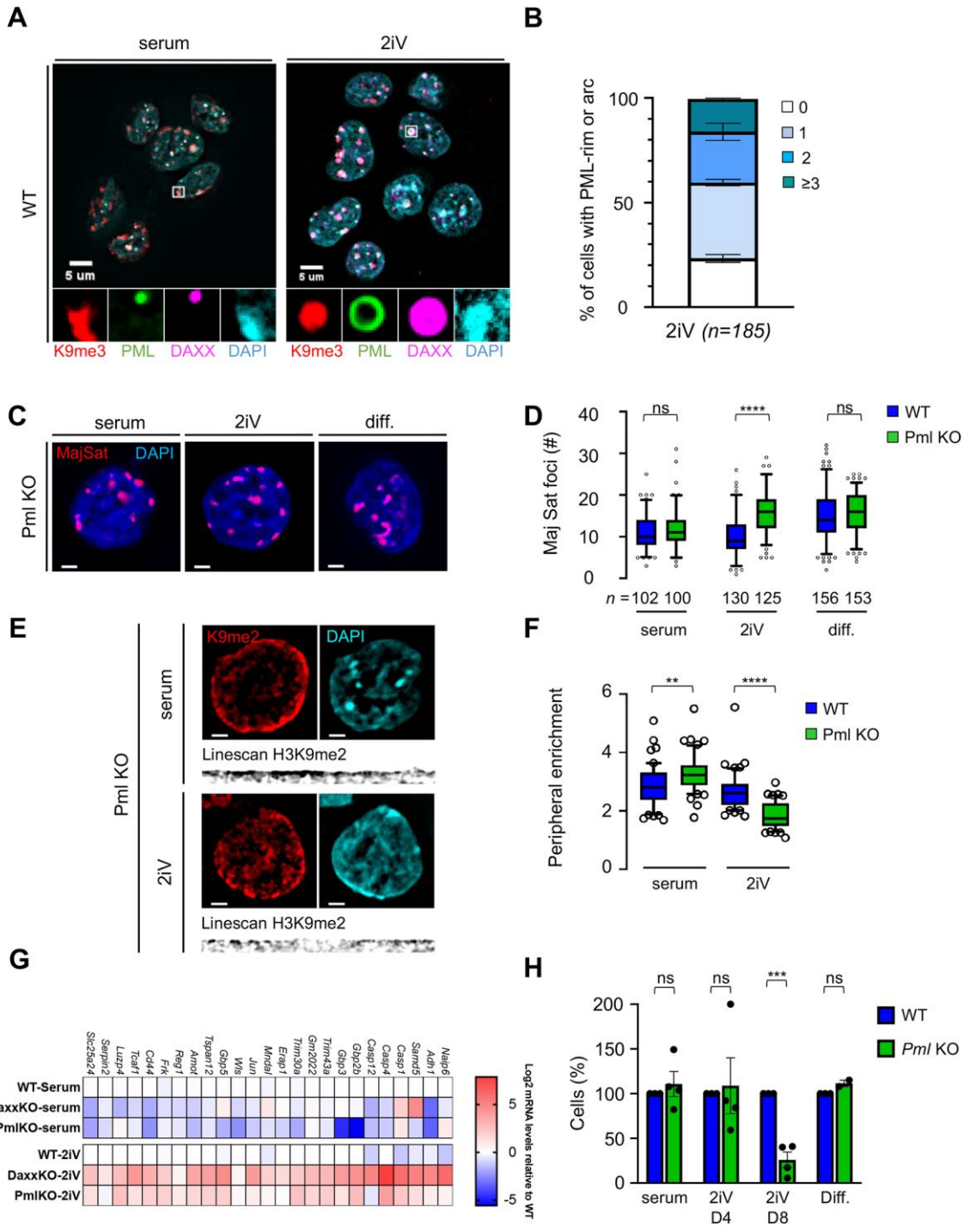

Fig. 5. PML protects heterochromatin in ground-state ESCs. (A) Representative field of WT ESCs grown in serum or 2iV immuno-detection of H3K9me3 (red), PML (green), DAXX (magenta) and counterstaining with DAPI (cyan). White squares highlight the absence (serum) or the presence (2iV) of PML-rim around H3K9me3 foci. **(B)** Stacked bar plots of the average fraction of cell population showing either 0, 1, 2 and 3 or more, PML-rims, with SEM, in 2i converted WT ESCs (n= total number of nuclei). **(C)** Representative major satellite DNA FISH pictures of *Pml* KO ESCs in serum, 2iV and differentiation (dif.) conditions. (scale bar =

2µm). **(D)** Quantification of the number of major satellite foci per nucleus. WT values (blue) are taken from Fig. 4B. n=total number of nuclei analyzed from at least 3 biological replicates. Two-sided Mann-Whitney tests were used for statistical analysis. ns, not significant; ****P<0.0001. **(E)** Representative nuclei immuno-detection of H3K9me2 (red) and counterstaining with DAPI (blue) in *Pml* KO ESCs grown in serum and 2iV (scale bar = 2µm). Linescan represent straighten H3K9me3 signal at the nuclear periphery (black). **(F)** Boxplot of H3K9me2 signal quantification enrichment at the nuclear periphery. WT values (blue) are taken from Fig. 1F. n=total number of nuclei analyzed from at least 3 biological replicates. Two-sided Mann-Whitney tests was used for statistical analysis. **P<0.01; ****P<0.0001. **(G)** Heatmap showing the average log2 fold changes in LAD gene expression for *Pml* KO and *Daxx* KO, compared to WT, in both serum and 2iV conditions. Data is derived from 3 biological replicates. **(H)** Quantification of the number of cells compared to WT in each culture condition. Bar plot represents mean with s.e.m. of 4 biological replicates. T-tests were used for statistical analysis. ns, not significant; ***P<0.001.

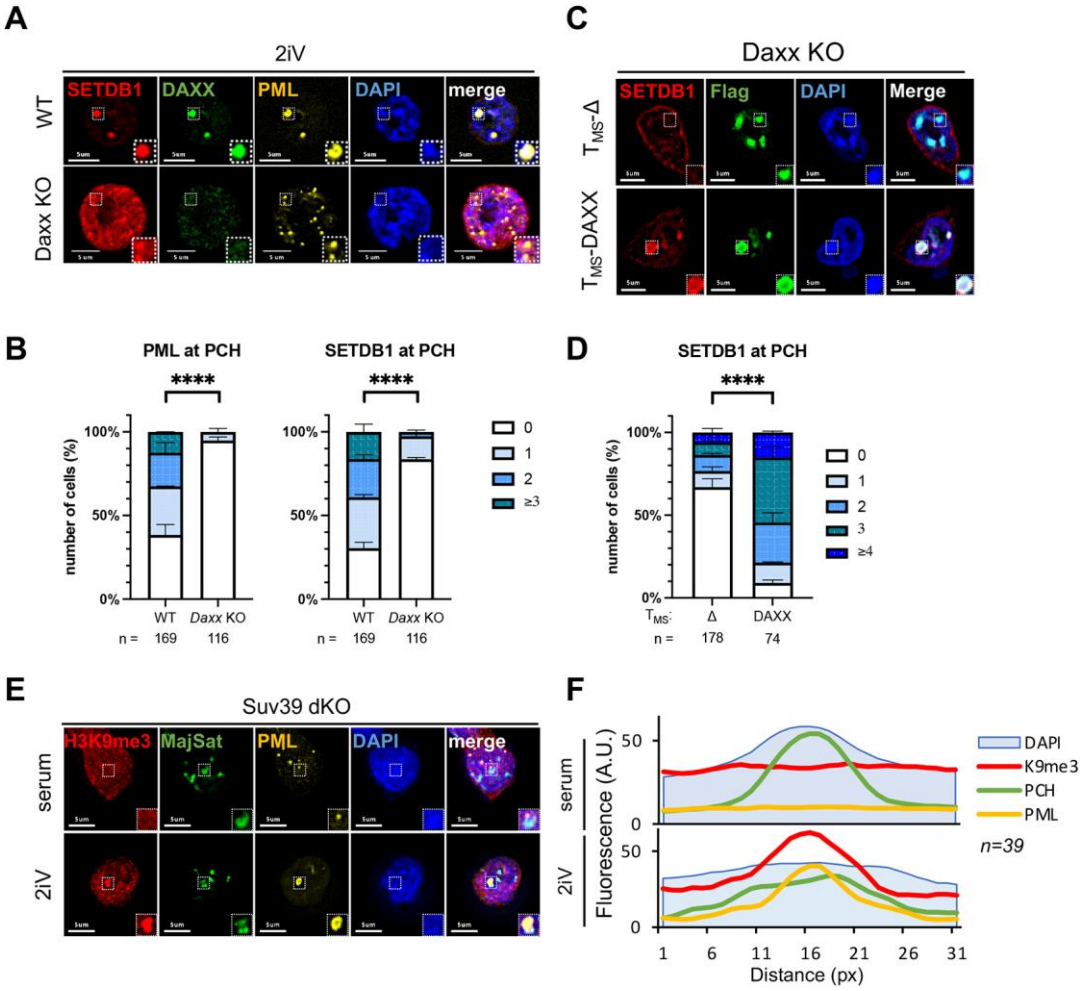

Fig. 6. DAXX recruits SETDB1 to PCH in ground-state ESCs. (A) Representative immunofluorescence pictures for SETDB1, DAXX and PML in WT or *Daxx* KO ESCs upon 2iV conversion. **(B)** Quantification of the mean number of PML or SETDB1 foci at chromocenters in WT and *Daxx* KO ESCs. n= total number of nuclei analyzed from two independent replicates. Chi-square tests were used for statistical analysis. ****P<0.0001. (**C)** Representative immunofluorescence pictures for SETDB1 and Flag-TALE in *Daxx* KO serum ESCs transfected with $TALE_{MajSat}$ (T_{MS}-Δ) or $TALE_{MajSat}$-DAXX (T_{MS}-DAXX). **(D)** Quantification of SETDB1 recruitment to Flag-positive chromocenters. The mean with s.e.m. from at least 2 biological replicates is shown. n=total number of nuclei analyzed. Chi-square tests were used for statistical analysis. ****P<0.0001. **(E)** Representative immunoFISH pictures for H3K9me3, PML and major satellites in 2iV and serum of Suv39dKO ESCs. White dashed squares highlight a major satellite focus. **(F)** Cumulated fluorescence intensities profile of H3K9me3 positive PCH foci in cells grown in serum or 2iV for either H3K9me3, PCH or PML signal. n=total number of nuclei analyzed from at least 2 biological replicates.

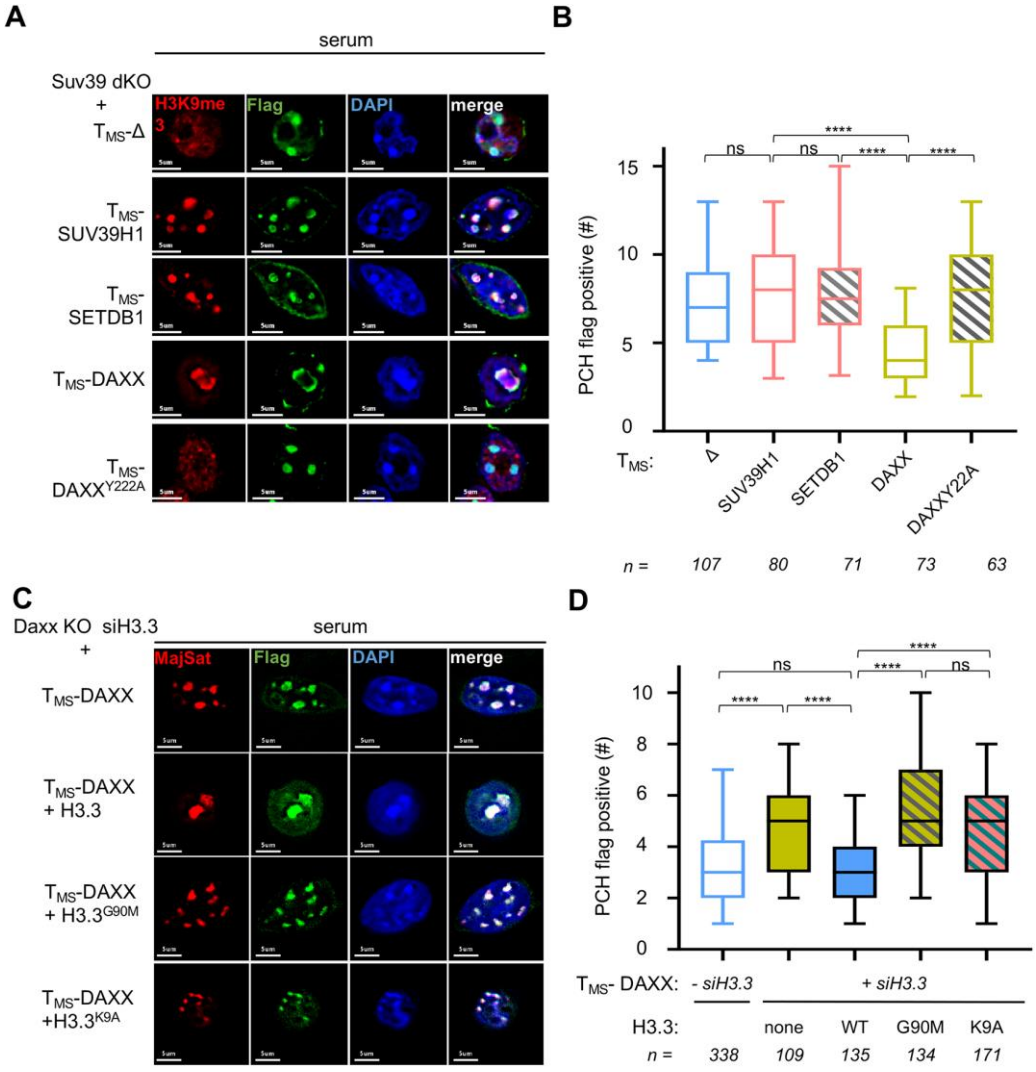

Fig. 7. The deposition of H3.3 and its modification on lysine 9 mediates PCH clustering. (A) Representative immunofluorescence pictures for H3K9me3 and Flag in Suv39dKO serum ESCs transfected with $TALE_{MajSat}$-Δ, $TALE_{MajSat}$-SUV39H1, $TALE_{MajSat}$-SETDB1, $TALE_{MajSat}$-DAXX or $TALE_{MajSat}$-$DAXX^{Y222A}$. **(B)** quantification of the number of PCH foci observed in the different transfection conditions described in (A). Two-sided Mann-Whitney tests were used for statistical analysis. ns, not significant; ****P<0.0001. **(C)** Representative immunoFISH pictures for major satellite and Flag in *Daxx* KO serum ESCs co-transfected with siRNA against H3.3, $TALE_{MajSat}$-DAXX and either no additional construct or H3.3WT, H3.3G90M or H3.3K9A. **(D)** Quantification of the number of major satellite foci detected of medium focal plane observed in the different transfection conditions described in (C). For comparison, distribution T_{MS}-DAXX without H3.3 knockdown data comes from Fig. 3D. n=total number of nuclei analyzed from 2 biological replicates. Two-sided Mann-Whitney tests were used for statistical analysis. ns, not significant; ****P<0.0001.

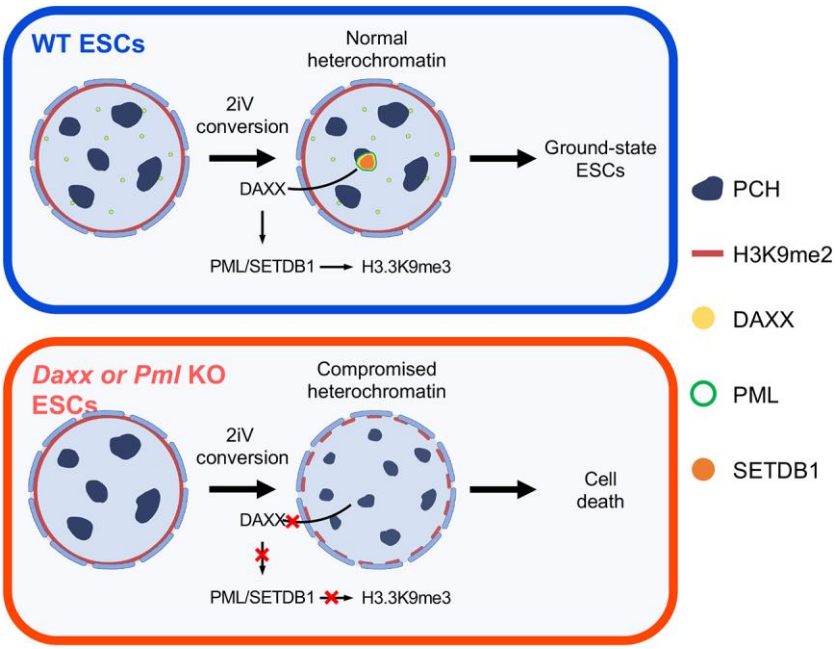

Fig. 8. Model for heterochromatin maintenance by DAXX in ESCs.

During ground-state conversion of ESCs, DAXX accumulates at PCH and is surrounded by a PML shell. DAXX recruits the histone methyltransferase SETDB1 to promote H3.3K9me3 to maintain the pericentromeric heterochromatin. In *Daxx* and *Pml* KO cells, the 3D-organization of heterochromatin is impaired. The peripheral heterochromatin H3K9me2 fails to accumulate properly at the nuclear edge leading to promiscuous expression of genes located in LADs. The clustering and the physical properties of pericentromeric heterochromatin is impacted, impairing transcriptional repression of major satellites. The global defect of heterochromatin observed in these cells prevents prolonged culture of these cells in ground-state condition.

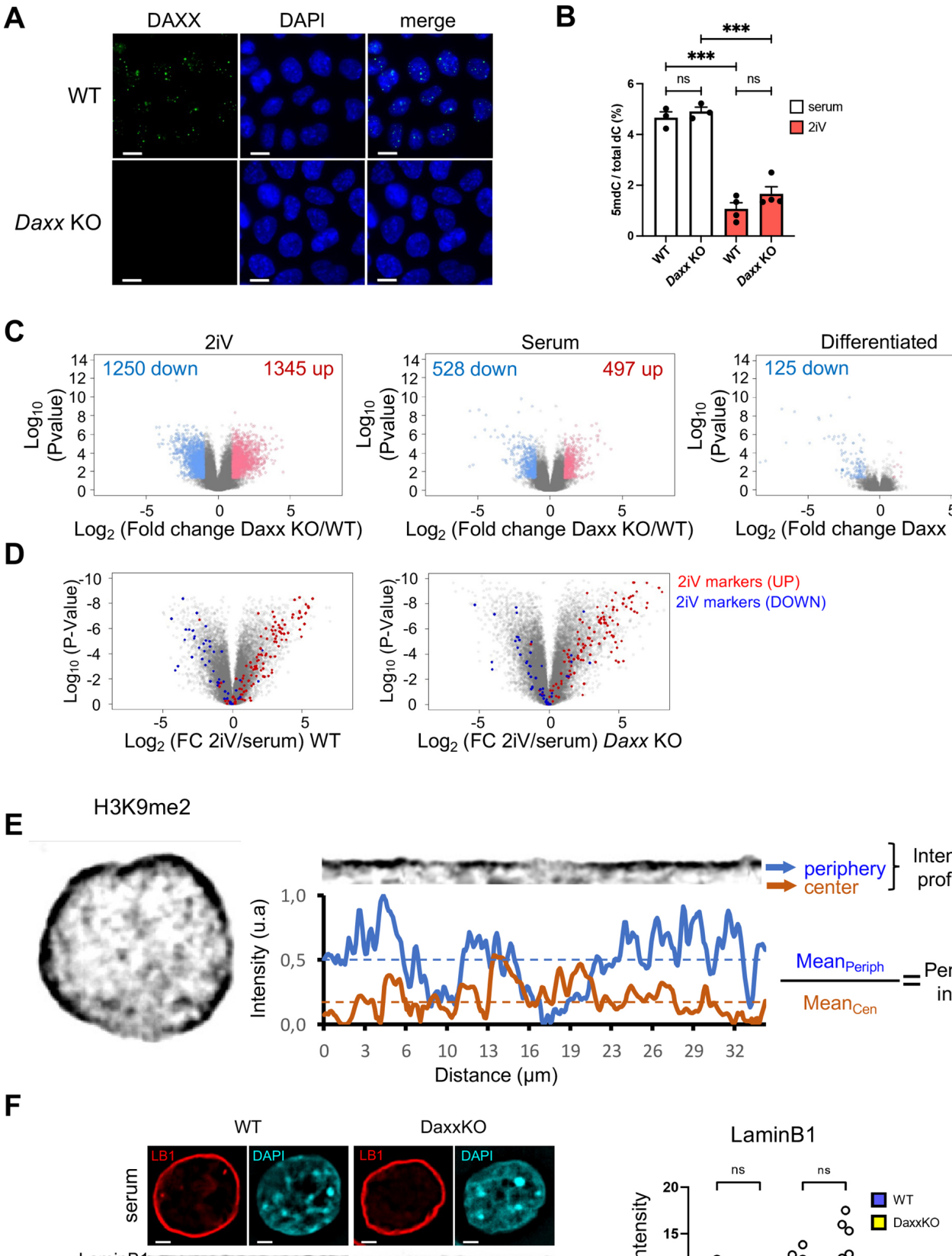

Fig. S1. Impact of *Daxx* deletion on ground-state conversion and nuclear periphery. (A) Representative field of WT and *Daxx* KO ESCs after IF against DAXX (green) and counterstaining with DAPI (blue). Scale bar = 10µm. **(B)** Quantitation of 5-mC abundance in the cells by LC-MS/MS. Error bars represent s.e.m. T-tests were used for statistical analysis. ns, not significant; ***P<0.001. **(C)** Volcano plot representing the number of differentially expressed genes in 2iV, serum or differentiated cells from RNA-seq experiments. Differentially expressed genes in red for down-regulated or blue for up-regulated correspond to Log2(FoldChange(KO/WT)) <-1 or >1 with p-value<0.05. **(D)** Volcano plots representing the number of differentially expressed genes upon 2iV conversion of WT and *Daxx* KO ESCs. Previously identified 2iV conversion markers are in red for up-regulated or blue for down-regulated (Blaschke et al., 2013). **(E)** Left, representative image of ESCs after IF against H3K9me2. Top right, linescan represents straighten H3K9me2 signal at the nuclear periphery (black). Bottom right, Intensity profiles of IF signals measured on linescans at the periphery (blue) or in the center (orange) of the nucleus. Ratio between mean intensity at the periphery and in the center was used to determined peripheral enrichment. **(F)** Left, representative nuclei after immuno-detection of LaminB1 (red) and counterstaining with DAPI (blue) in WT and *Daxx* KO ESCs in serum and 2iV (scale bar = 2µm). Linescan represent straighten LaminB1 signal at the nuclear periphery (black). Right, boxplots of LaminB1 signal quantification enrichment at the nuclear periphery from 2 independent replicates. Two-sided Mann-Whitney tests were used for statistical analysis. ns, not significant.

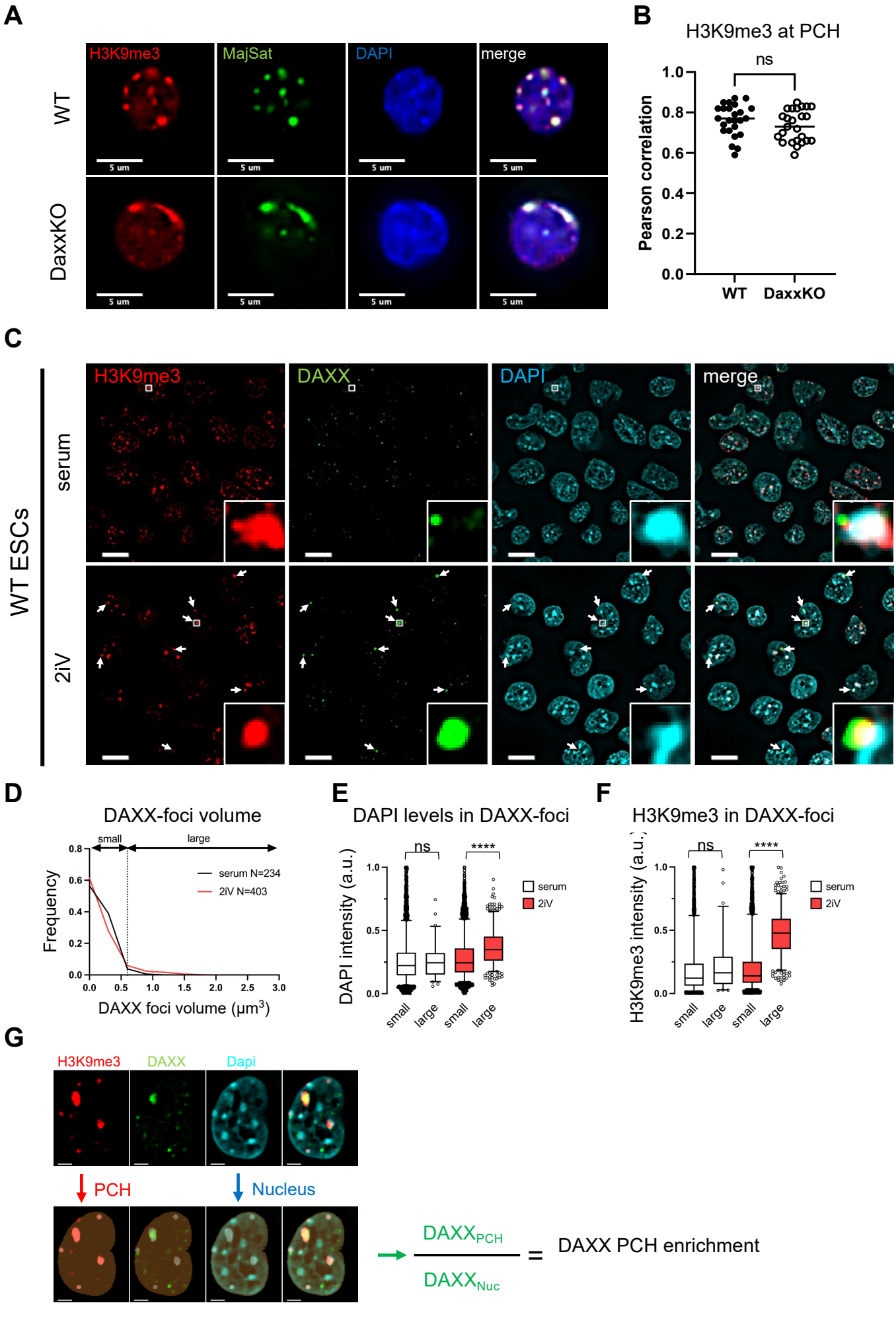

Fig. S2. Quantification of DAXX at chromocenters. (A) Representative immunoFISH picture with H3K9me3 and major satellites DNA. **(B)** Dot plots of Pearson correlation between H3K9me3 and major satellite signals. Two-sided Mann-Whitney tests was used for statistical analysis. ns, not significant. **(C)** Representative field of ESCs grown in serum or 2iV immuno-detection of H3K9me3 (red), DAXX (green) and counterstaining with DAPI (cyan). White squares and arrows highlight the presence (2iV) of larger DAXX foci with higher levels of H3K9me3 and DAPI. Scale bar = 10µm. **(D)** Distribution of DAXX foci volume observed in WT ESCs grown in serum (black) or in 2iV (red) from 3 independent replicates. Dashed line indicates the threshold used to defined large or small DAXX foci. **(E)** Boxplot of DAPI signal intensity observed under small and large DAXX foci in serum (white) and 2iV (red) conditions. Two-sided Mann-Whitney tests were used for statistical analysis. ns, not significant; ****P<0.0001. **(F)** Boxplot of H3K9me3 signal intensity observed under small and large DAXX foci in serum (white) and 2iV (red) conditions. Two-sided Mann-Whitney tests were used for statistical analysis. ns, not significant; ****P<0.0001. **(G)** Top, ESCs nucleus after immuno-detection of H3K9me3, DAXX and counterstaining with DAPI. Bottom, for each nucleus, H3K9me3 and DAPI signals were segmented to PCH and nuclear ROIs. DAXX enrichment at PCH was defined by the ratio of DAXX intensity under PCH ROIs (scale bar = 2µm).

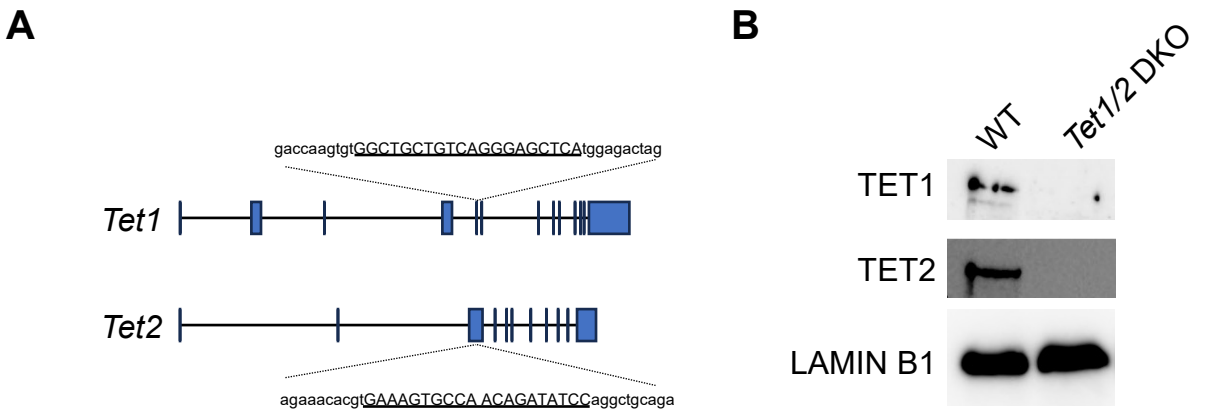

Fig. S3. Strategy and Validation for Tet1 and Tet2 Deletion in ESCs. (A) Schematic of the *Tet1* and *Tet2* loci and the of the sequences of each guide RNA. **(B)** Western blot with anti-TET1 and anti-TET2 antibodies, anti-LAMIN-B1 served as loading control.

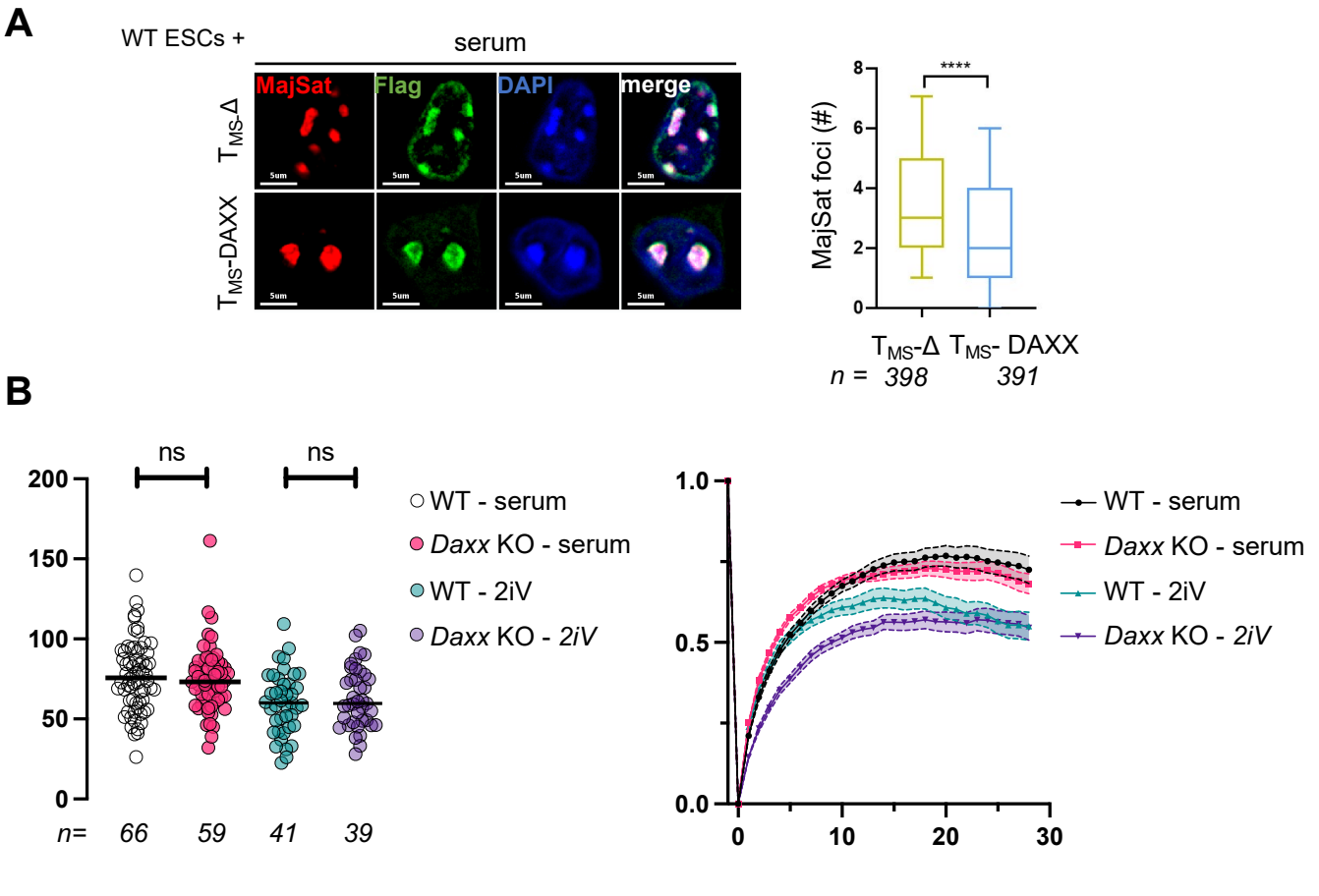

Fig. S4. Role of DAXX on pericentromeric heterochromatin formation. (A) Left, representative immunoFISH pictures for major satellites and Flag for WT ESCs, grown in serum, transfected with $TALE_{MajSat}$-Δ or $TALE_{MajSat}$-DAXX. Right, quantification of the number of major satellite foci detected in the focal plane and corresponding surface area. n=total number of nuclei for number and foci for sizes analyzed. Two-sided Mann-Whitney tests was used for statistical analysis. ****P<0.0001. **(B)** Left, mobile fractions of GFP-HP1α calculated from data presented in Fig. 4E. n=total number of cells analyzed from 2 biological replicates. Right, fluorescence recovery curves generated for FRAP experiments in WT or *Daxx* KO cells in serum or ground-state condition. Two-sided Mann-Whitney tests were used for statistical analysis. ns, not significant. **(C)** MNAse digestion for indicated times in minutes (min.) in WT or *Daxx* KO cell lines. Total DNA is revealed on a BET agarose gel and Major satellites via a Southern blot experiment. Right, intensity values of total DNA or major satellite signals, according to fragment size, from 4min of MNase digestion. Two experiments from two biological replicates are shown.

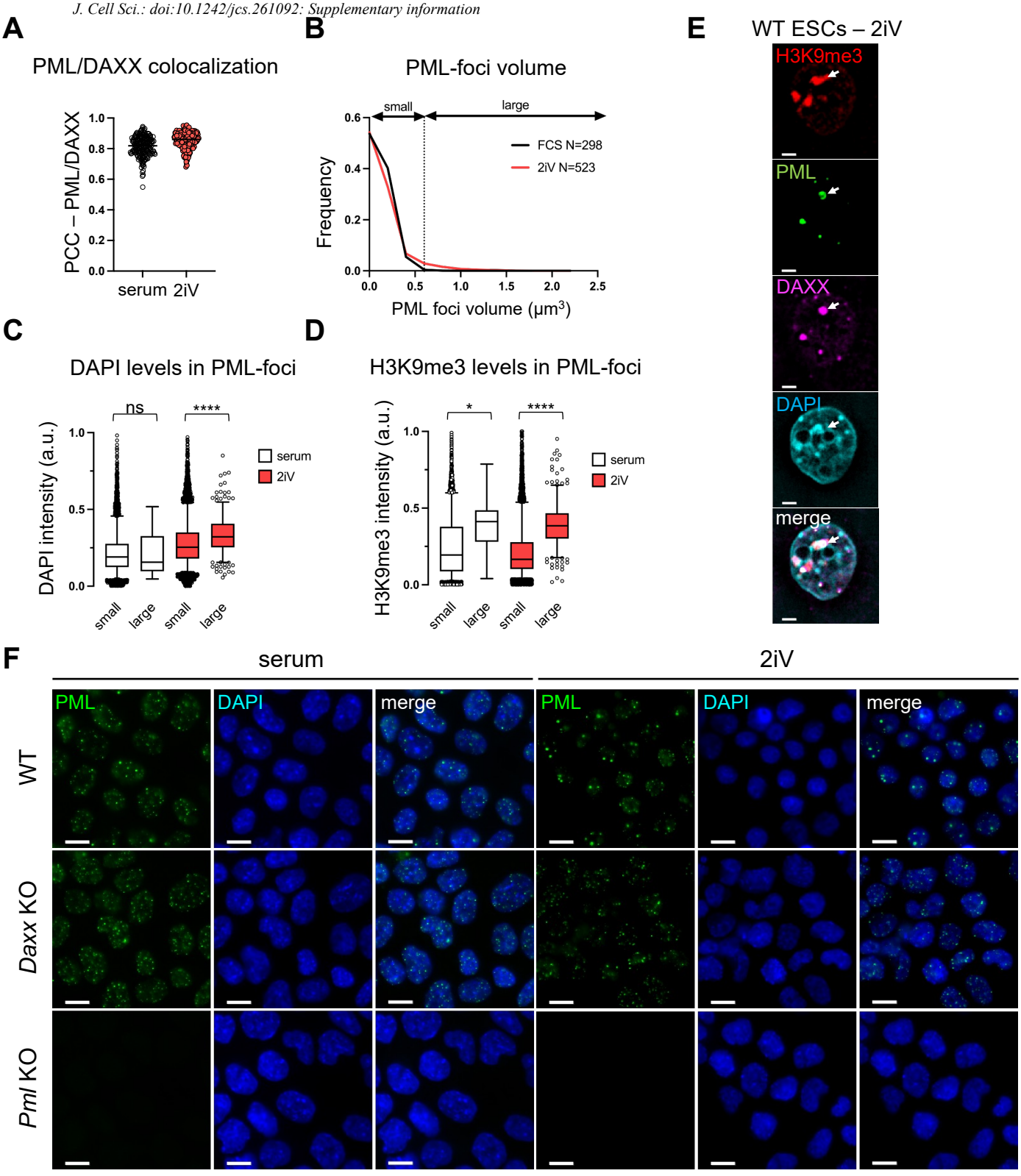

Fig. S5. Role of PML at heterochromatin. (A) Quantification of the Pearson's Correlation Coefficients (PCC) between PML and DAXX immunofluorescence signals under serum and 2iV conditions. **(B)** Distribution of PML foci volume observed in WT ESCs grown in serum (black) or in 2iV (red) from 3 independent replicates. Dashed line indicates the threshold used to defined large PML foci. **(C)** Boxplot of DAPI signals intensities observed under small and large PML foci in serum (white) and 2iV (red) conditions. Two-sided Mann-Whitney tests were used for statistical analysis. ns, not significant; ****P<0.0001. **(D)** Boxplot of H3K9me3 signals intensities observed under small and large PML foci in serum (white) and 2iV (red) conditions. Two-sided Mann-Whitney tests were used for statistical analysis. *P<0.05; ****P<0.0001. **(E)** Representative nucleus of ESCs grown in 2iV after immuno-detection of H3K9me3, PML, DAXX and counterstaining with DAPI (cyan) presenting a PML-arc around a PCH cluster (white arrow). Scale bar = 2µm. Two-sided Mann-Whitney tests were used for statistical analysis in B and D. **(F)** Representative field of WT, *Daxx* KO and *Pml* KO ESCs, in serum or 2iV after IF against PML (green) and counterstaining with DAPI (blue). Scale bar = 10µm. **(G)** Representative nuclei after immuno-detection of LaminB1 (red) and counterstaining with DAPI (blue) in WT and *Pml* KO ESCs in serum and 2iV (scale bar = 2µm). Linescans represent straighten LaminB1 signal at the nuclear periphery (black). **(H)** Boxplot of LaminB1 signal quantification enrichment at the nuclear periphery from 2 independent replicates. WT values are taken from Fig. S2D. Two-sided Mann-Whitney tests were used for statistical analysis. ns, not significant.

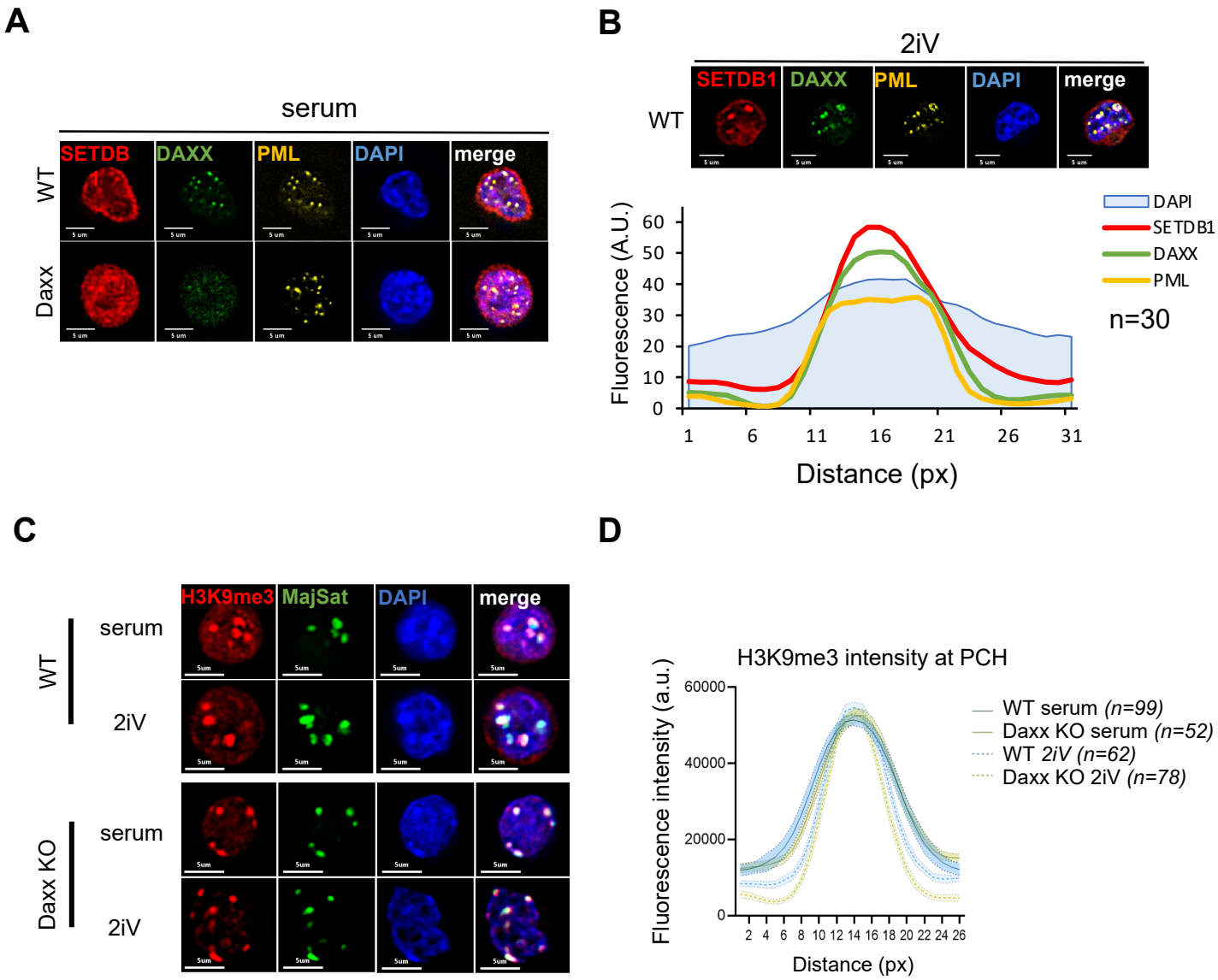

Fig. S6. DAXX recruits SETDB1 to pericentromeres. (A) Representative immunofluorescence pictures for SETDB1, DAXX and PML in WT or *Daxx* KO ESCs in serum condition. **(B)** Top, representative immunofluorescence pictures for SETDB1, DAXX and PML in WT ESCs in 2iV. Bottom, cumulated fluorescence intensities profile of PCH foci for either SETDB1, DAXX or PML signal. n=total number of nuclei analyzed from at least 2 biological replicates. **(C)** Representative immunoFISH pictures for H3K9me3 and DNA FISH of major satellites (MajSat) in both WT and *Daxx* KO ESCs in serum or ground-state (2iV) conditions. **(D)** Mean and SEM of fluorescence intensity of H3K9me3 measured over major satellite signal. n=total number of nuclei analyzed from two independent replicates. **(E)** Quantification of the percentage of Flag-DAPI-dense PCH displaying H3K9me3 recruitment at in Suv39dKO serum ESCs transfected with $TALE_{MajSat}$-Δ, $TALE_{MajSat}$-SUV39H1, $TALE_{MajSat}$-SETDB1 or $TALE_{MajSat}$-DAXX.

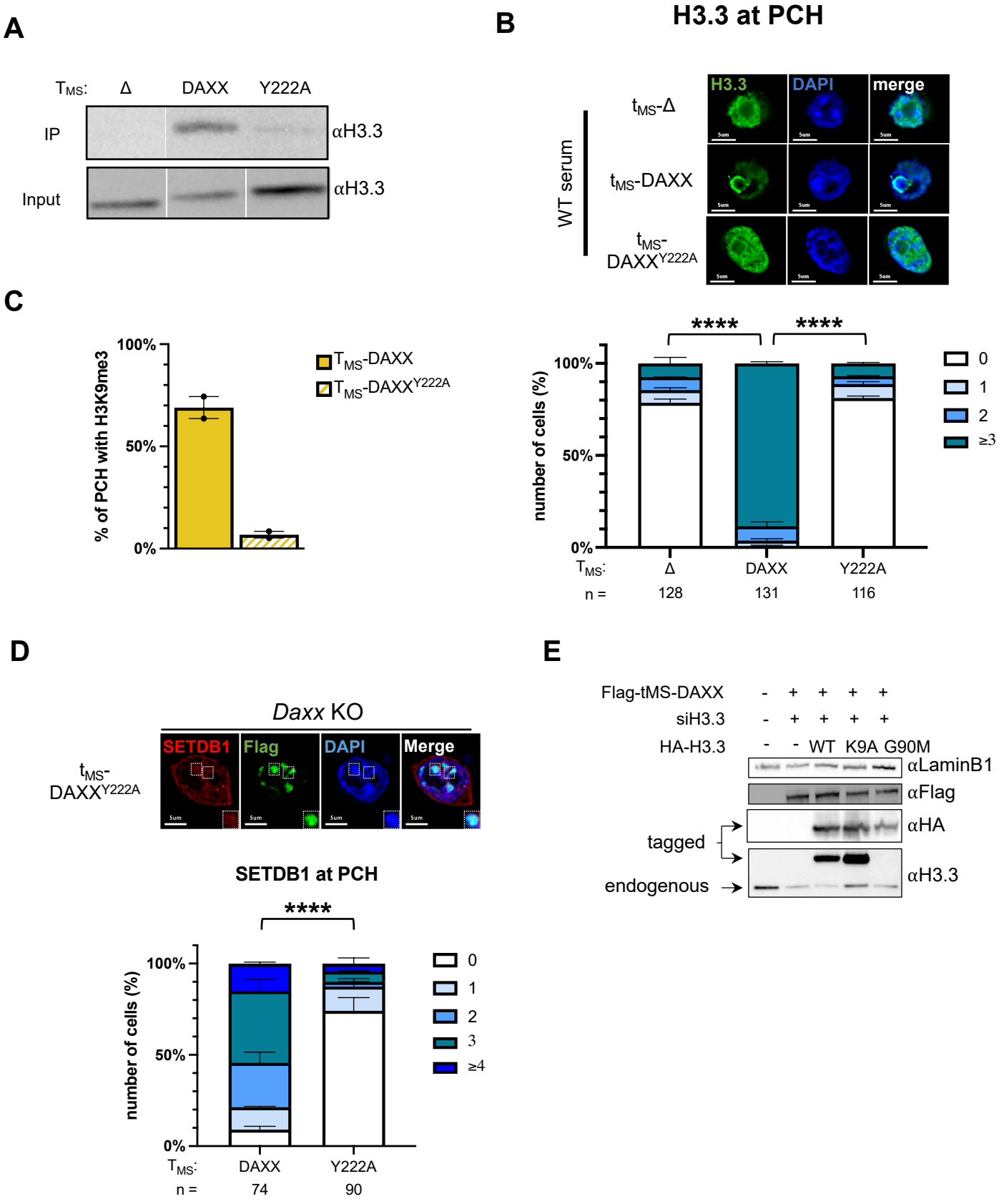

Fig. S7. Role of H3.3 and H3K9me3 modifications at PCH. (A) Represents signal after Flag-TALE immunoprecipitation. Bottom line represents input line from total extract. **(B)** Top, representative immunofluorescence pictures of HA-H3.3 in WT cells grown in serum transfected with $TALE_{MajSat}$-Δ, $TALE_{MajSat}$-DAXX or $TALE_{MajSat}$-$DAXX^{Y222A}$. Bottom, quantification of H3.3 recruitment at DAPI-dense chromocenters in the indicated Tale-transfected cells. Means are represented with s.e.m. from at least 2 biological replicates. n=total number of nuclei analyzed. Chi-square tests was used for statistical analysis. ****P<0.0001. **(C)** Quantification of the percentage of Flag-DAPI-dense PCH displaying H3K9me3 recruitment at in Suv39dKO serum ESCs transfected with T_{MS}-DAXX or T_{MS}-$DAXX^{Y222A}$. Data from T_{MS}-DAXX are taken from Fig. S6E. (**D)** Top Representative immunofluorescence pictures for SETDB1 and Flag-TALE in *Daxx* KO serum ESCs transfected with T_{MS}-$DAXX^{Y222A}$. White dashed squares highlight DAPI-dense Flag-positive chromocenters. Bottom, quantification of SETDB1 recruitment to Flag-positive chromocenters. Means are represented with s.e.m. from at least 2 biological replicates. For comparison, distribution from T_{MS}-DAXX transfection comes from Fig. 6D. n=total number of nuclei analyzed. Chi-square tests was used for statistical analysis. ****P<0.0001. **(E)** Western blot showing the amount of TALE and H3.3 variants in *Daxx* KO ESCs grown in serum transfected with the indicated constructions.

Table S1. oligonucleotide sets used in this study. Abbreviations; Sg. Small guide RNA, Exp. Expression, F. forward, R. reverse.

Primers	Sequence (5'-3')	Application
Sg-mDaxx	gGACCTCATCCAGCCGGTTCA	Crispr-Cas9
Sg-Tet1	GGCTGCTGTCAGGGAGCTCA	Crispr-Cas9
Sg-Tet2	GAAAGTGCCAACAGATATCC	Crispr-Cas9
exp-GAPDH-F	ATCACCATCTTCCAGGAGCGAG	RT-qPCR
exp-GAPDH-R	GACCCTTTTGGCTCCACCCTTC	RT-qPCR
exp-mDAXX-F	GAGGGCGAGAGACAGAAGAG	RT-qPCR
exp-mDAXX-R	GTCGTCGTCATCATCATCGT	RT-qPCR
exp-MajSat-F	TGGAATATGGCGAGAAAACTG	RT-qPCR
exp-MajSat-R	AGGTCCTTCAGTGGGCATTT	RT-qPCR
Exp-Gbp2b-F	AAGGGCATCTGGATGTGGTG	RT-qPCR
Exp-Gbp2b-R	GATGAAGGTGCTGCTGAGGA	RT-qPCR
Exp-Gbp3-F	ACACACCCTGGTCCTTTTGG	RT-qPCR
Exp-Gbp3-R	TGCTGGTTGATGGTGCTCAT	RT-qPCR
Exp-Trim43a-F	TGGTCACACACACTGTTCCA	RT-qPCR
Exp-Trim43a-R	TAGCTTCACGGACAACCACC	RT-qPCR
Exp-Gm2022-F	TGAAGCAAGAAGTCTGAAGGC	RT-qPCR
Exp-Gm2022-R	TCATCATCATCCCCAGGACCA	RT-qPCR
Exp-Trim30a-F	GGAGCTCTGTGGAAGCTGAT	RT-qPCR
Exp-Trim30a-R	TCTCCTTGGAGTCCAGGAGG	RT-qPCR
Exp-Ifi44-F	TCCAACTGACTGCTCGCAAT	RT-qPCR
Exp-Ifi44-R	ACCAGGTCTCCATAGGGCTT	RT-qPCR
Exp-Erap1-F	GCCGATTATGCTCTGGATGC	RT-qPCR
Exp-Erap1-R	GGTCAGTCCCCAGTTTTCCA	RT-qPCR
Exp-Mndal-F	TGTGAAGAACCCACAGCCAG	RT-qPCR
Exp-Mndal-R	CATCACTGTCAGGGGCTCTG	RT-qPCR
Exp-Jun-F	TCTGGCTATGCAGTTCAGCC	RT-qPCR
Exp-Jun-R	TGGGCACATCACCACTACAC	RT-qPCR
Exp-Gbp5-F	GCTTCCAACACTCAGCAACG	RT-qPCR
Exp-Gbp5-R	GGCTTTCTAGACGAGGTCCG	RT-qPCR
Exp-Tspan12-F	GTGGACATACGAGCAGGAGG	RT-qPCR
Exp-Tspan12-R	GTACACCACTCCACAGCACT	RT-qPCR
Exp-Amot-F	AGCTGGAGGGCGAGATTAGA	RT-qPCR
Exp-Amot-R	ATGTTTGGCAAAGAGCTGCG	RT-qPCR
Exp-Wls-F	TGGTGTGGTATTGGAGGAGGA	RT-qPCR
Exp-Wls-R	CAGCATCCAGGTCCAGTCAA	RT-qPCR
Exp-Reg1-F	CCCAGAAGGTTCCAATGCCT	RT-qPCR
Exp-Reg1-R	AGAGAGGCCACAAAGTTGCC	RT-qPCR
Exp-Frk-F	AAGGTTGGATGAAGGTGGCT	RT-qPCR
Exp-Frk-R	AGGGGTTGGTACCTGGATCT	RT-qPCR
Exp-Cd44-F	CCTTCGATGGACCGGTTACC	RT-qPCR
Exp-Cd44-R	CTCTTCTCGATGGTGGAGCC	RT-qPCR
Exp-Tcaf1-F	GGGTTCTGTGCCCCTTACAG	RT-qPCR
Exp-Tcaf1-R	CAGTGGGCACAGTCAGGATG	RT-qPCR
Exp-Luzp4-F	AGAAATGGACCAAGGGATGCA	RT-qPCR
Exp-Luzp4-R	AGCCGTCTTCTAGCCCTACA	RT-qPCR
Exp-Serpine2-F	CCTCTGCCTCTGAGTCCATC	RT-qPCR
Exp-Serpine2-R	ACCGAGACTTCCACAAACCC	RT-qPCR
Exp-Slc25a24-F	CCTCAAGGTCATGATGCAGGT	RT-qPCR
Exp-Slc25a24-R	CCCAGAACTTCACAGCTGTCT	RT-qPCR
exp-Samd5-F	CTGAGCAAACCCCCATACTC	RT-qPCR
exp-Samd5-R	ATACGCCCCTTTCCAGTCTT	RT-qPCR
exp-Naip6-F	CGACATCTTGGACGATGAAA	RT-qPCR
exp-Naip6-R	GTTGTCCAGGGCTTGAAAGA	RT-qPCR
exp-Adh1-F	TGTGGCTGACTTCATGGCTA	RT-qPCR
exp-Adh1-R	AAGTCAGGACGGTACGGATG	RT-qPCR
exp-Casp1-F	CGTCTTGCCCTCATTATCTGC	RT-qPCR
exp-Casp1-r	CACCATCTCCAGAGCTGTGA	RT-qPCR
exp-Casp4-F	TCTCACTGAGGTATGGGGCT	RT-qPCR
exp-Casp4-R	GTCTGGTGTTCTGAGAGTGCA	RT-qPCR
exp-Cas12-F	CGAACACGTCTGGCTCTCAT	RT-qPCR
exp-Cas12-R	TGTCTCCATTTCCTGAGCTGT	RT-qPCR